

# VALES V: A kinematic analysis of the molecular gas content in *H*-ATLAS galaxies at $z \sim 0.03 - 0.35$ using ALMA

J. Molina,<sup>1\*</sup> Edo Ibar,<sup>2</sup> V. Villanueva,<sup>3</sup> A. Escala,<sup>1</sup> C. Cheng,<sup>2,4</sup> M. Baes,<sup>5</sup>  
 H. Messias,<sup>6,7</sup> C. Yang,<sup>7</sup> F. E. Bauer,<sup>8,9,10</sup> P. van der Werf,<sup>11</sup> R. Leiton,<sup>2</sup>  
 M. Aravena,<sup>12</sup> A. M. Swinbank,<sup>13,14</sup> M. J. Michałowski,<sup>15</sup> A. M. Muñoz-Arancibia,<sup>2</sup>  
 G. Orellana,<sup>2</sup> T. M. Hughes,<sup>2,16,17,18</sup> D. Farrah,<sup>19,20</sup> G. De Zotti,<sup>21</sup> M. A. Lara-López,<sup>22</sup>  
 S. Eales,<sup>23</sup> L. Dunne.<sup>23,24</sup>

<sup>1</sup>Departamento de Astronomía, Universidad de Chile, Casilla 36-D, Santiago, Chile.

<sup>2</sup>Instituto de Física y Astronomía, Universidad de Valparaíso, Avda. Gran Bretaña 1111, Valparaíso, Chile

<sup>3</sup>Department of Astronomy, University of Maryland, College Park, MD 20742, USA

<sup>4</sup>CASSACA, National Astronomical Observatories, Chinese Academy of Sciences, Beijing 100012, China

<sup>5</sup>Sterrenkundig Observatorium, Universiteit Gent, Krijgslaan 281 S9, B-9000 Gent, Belgium

<sup>6</sup>Joint ALMA Observatory, Alonso de Córdova 3107, Vitacura 763-0355, Santiago, Chile

<sup>7</sup>European Southern Observatory, Alonso de Córdova 3107, Casilla 19001, Vitacura, Santiago, Chile

<sup>8</sup>Instituto de Astrofísica, Facultad de Física, Pontificia Universidad Católica de Chile, 306, Santiago 22, Chile

<sup>9</sup>Millennium Institute of Astrophysics (MAS), Nuncio Monseñor Sótero Sanz 100, Providencia, Santiago, Chile

<sup>10</sup>Space Science Institute, 4750 Walnut Street, Suite 205, Boulder, Colorado 80301

<sup>11</sup>Leiden Observatory, Leiden University, P.O. Box 9513, NL-2300 RA Leiden, The Netherlands

<sup>12</sup>Núcleo de Astronomía, Facultad de Ingeniería y Ciencias, Universidad Diego Portales, Av. Ejército 441, Santiago, Chile

<sup>13</sup>Centre for Extragalactic Astronomy, Department of Physics, Durham University, South Road, Durham DH1 3LE, UK

<sup>14</sup>Institute for Computational Cosmology, Durham University, South Road, Durham DH1 3LE, UK

<sup>15</sup>Astronomical Observatory Institute, Faculty of Physics, Adam Mickiewicz University, ul. Stoleczna 36, 60-286 Poznań, Poland

<sup>16</sup>CAS Key Laboratory for Research in Galaxies and Cosmology, Department of Astronomy, University of Science and Technology of China, Hefei 230026, China

<sup>17</sup>School of Astronomy and Space Science, University of Science and Technology of China, Hefei 230026, China

<sup>18</sup>Chinese Academy of Sciences South America Center for Astronomy, China-Chile Joint Center for Astronomy, Camino El Observatorio #1515, Las Condes, Santiago, Chile

<sup>19</sup>Department of Physics and Astronomy, University of Hawaii, 2505 Correa Road, Honolulu, HI 96822, USA

<sup>20</sup>Institute for Astronomy, 2680 Woodlawn Drive, University of Hawaii, Honolulu, HI 96822, USA

<sup>21</sup>INAF, Osservatorio Astronomico di Padova, Vicolo dell'Osservatorio 5, I-35122 Padova, Italy

<sup>22</sup>Dark Cosmology Centre, Niels Bohr Institute, University of Copenhagen, Juliane Maries Vej 30, DK-2100 Copenhagen, Denmark

<sup>23</sup>School of Physics and Astronomy, Cardiff University, Queens Buildings, The Parade, Cardiff CF24 3AA, UK

<sup>24</sup>Institute for Astronomy, University of Edinburgh, Royal Observatory, Blackford Hill, Edinburgh EH9 3HJ, UK

Accepted XXX. Received YYY; in original form ZZZ

## ABSTRACT

We present Atacama Large Millimeter/submillimeter Array (ALMA) resolved observations of molecular gas in galaxies up to  $z = 0.35$  to characterise the role of global galactic dynamics on the global interstellar medium (ISM) properties. These observations consist of a sub-sample of 39 galaxies taken from the Valparaíso ALMA Line Emission Survey (VALES). From the CO( $J = 1 - 0$ ) emission line, we quantify the kinematic parameters by modelling the velocity fields. We find that the IR luminosity increases with the rotational to dispersion velocity ratio ( $V_{\text{rot}}/\sigma_v$ , corrected for inclination). We find a dependence between  $V_{\text{rot}}/\sigma_v$  and the [CII]/IR ratio, suggesting that the so-called ‘[CII] deficit’ is related to the dynamical state of the galaxies. We find that global pressure support is needed to reconcile the dynamical mass estimates with the stellar masses in our systems with low  $V_{\text{rot}}/\sigma_v$  values. The star formation rate (SFR) is weakly correlated with the molecular gas fraction ( $f_{\text{H}_2}$ ) in our sample, suggesting that the release of gravitational energy from cold gas may not be the main energy source of the turbulent motions seen in the VALES galaxies. By defining a proxy of the ‘star formation efficiency’ parameter as the SFR divided by the CO luminosity ( $\text{SFE}' \equiv \text{SFR}/L'_{\text{CO}}$ ), we find a constant  $\text{SFE}'$  per crossing time ( $t_{\text{cross}}$ ). We suggest that  $t_{\text{cross}}$  may be the controlling timescale in which the star formation occurs in dusty  $z \sim 0.03 - 0.35$  galaxies.

**Key words:** galaxies: ISM – galaxies: star formation – galaxies: kinematics and dynamics – galaxies: evolution

## 1 INTRODUCTION

The star formation activity is one of the main processes that drives cosmic evolution of galaxies. Stars produce heavy elements via nucleosynthesis, which are expelled into the ISM during their late stages of evolution, enriching the gas with metals and dust (see e.g. [Nozawa & Kozasa 2013](#)). Thus, star formation is directly involved in the processes the growth and evolution of galaxies to the formation of planets through cosmic time. Nevertheless, our knowledge about the physical processes that dominate the formation of stars starting from pristine gas is far from complete, mainly because of the wide range of physical processes are involved.

[Schmidt \(1959\)](#) was the first to propose a power-law relationship between the star formation activity of galaxies and their gas content. This relationship was confirmed later by [Kennicutt \(1998a,b\)](#), who revealed a clear relationship between the disk-averaged total galaxy gas (atomic plus molecular) surface density ( $\Sigma_{\text{gas}}$ ) and the rate of star formation per surface area ( $\Sigma_{\text{SFR}}$ ), the Kennicutt-Schmidt relationship (hereafter, KS law). The KS law describes how efficiently galaxies turn their gas into stars. It has been used to constrain theoretical models and as a critical input to numerical simulations for galaxy evolution models (e.g. [Springel & Hernquist 2003](#); [Krumholz & McKee 2005](#); [Vogelsberger et al. 2014](#); [Schaye et al. 2015](#)). Using this relationship we can compute the time at which a given galaxy would convert all of its current gas mass content  $M_{\text{gas}}$  if it maintains its present star formation rate (SFR), this timescale is called the depletion time:  $t_{\text{dep}} \equiv M_{\text{gas}}/\text{SFR}$ .

Since [Kennicutt \(1998a,b\)](#)'s work, the KS law has been tested in numerous spatially-resolved surveys on local galaxies during the last decades (e.g. [Wong & Blitz 2002](#); [Kennicutt et al. 2007](#); [Bigiel et al. 2008](#); [Villanueva et al. 2017](#)). These surveys have allowed us to trace the SFR surface density ( $\Sigma_{\text{SFR}}$ ), atomic gas surface density ( $\Sigma_{\text{HI}}$ ), molecular gas surface density ( $\Sigma_{\text{H}_2}$ ) and study how these quantities relate to each other (e.g. [Leroy et al. 2008, 2013](#)). One of the first conclusions extracted from these observations was that star formation in galaxies is more strongly correlated with  $\Sigma_{\text{H}_2}$  than  $\Sigma_{\text{HI}}$  (especially at  $\Sigma_{\text{gas}} > 10 M_{\odot} \text{pc}^{-2}$ ), with an observed molecular gas depletion time of  $t_{\text{dep}} \approx 1 - 2 \text{ Gyr}$ .

When additional data from high star-forming galaxies are included, the KS law shows an apparent bimodal behaviour where ‘disks’ and ‘starburst’ galaxies appear to fill the  $\Sigma_{\text{H}_2} - \Sigma_{\text{SFR}}$  plane in different loci ([Daddi et al. 2010](#)). Nevertheless, by comparing  $\Sigma_{\text{SFR}}$  with  $\Sigma_{\text{H}_2}$  per galaxy free-fall time ( $t_{\text{ff}}$ ) and/or orbital time ( $t_{\text{orb}}$ ) a single power-law relationship can be recovered (e.g. [Daddi et al. 2010](#); [Krumholz, Dekel & McKee 2012](#)). The  $\Sigma_{\text{SFR}} - \Sigma_{\text{H}_2}/t_{\text{ff}}$  relation can be interpreted as dependence of the star formation law on the local volume density of the gas, whilst the  $\Sigma_{\text{SFR}} - \Sigma_{\text{H}_2}/t_{\text{orb}}$  relation suggests that the star formation law is affected by the global rotation of the galaxy. Thus, the relevant timescale gives us critical information about the physical processes that may control the formation of stars.

However, by exploiting the VALES survey in the local Universe ( $z < 0.3$ ; see § 2.1), [Cheng et al. \(2018\)](#) showed that the bimodality seen in the KS law may also be the result of the assumptions, and thus, the uncertainties behind the estimates of the molecular gas mass ( $M_{\text{H}_2}$ ).

The absence of an electric dipole moment in the hy-

drogen molecule ( $\text{H}_2$ ) implies that direct detections of cold  $\text{H}_2$  gas are difficult to be obtained (e.g. [Papadopoulos & Seaquist 1999](#); [Bothwell et al. 2013](#)) and tracers of the molecular gas are needed. One of the methods –and perhaps the most common one– to estimate the molecular gas content is through the carbon monoxide ( $^{12}\text{C}^{16}\text{O}$ , hereafter CO) line luminosity (e.g. [Solomon et al. 1987](#); [Downes & Solomon 1998](#); [Solomon & Vanden Bout 2005](#); [Bolatto et al. 2013](#)) of rotational low- $J$  transitions (e.g.  $J = 1 - 0$  or  $J = 2 - 1$ ). Because the CO emission line is generally optically thick ( $\tau_{\text{CO}} \approx 1$ ), its brightness temperature ( $T_{\text{b}}$ ) is related to the temperature of the optically thick gas sheet, not the column density of the gas. Thus the mass of the self gravitating entity, such as a molecular cloud, is related to the emission line-width, which reflects the velocity dispersion of the gas ([Bolatto et al. 2013](#)).

Assuming that the CO luminosity ( $L'_{\text{CO}}$ ) of an entire galaxy comes from an ensemble of non-overlapping virialized emitting clouds, then if: (1) the intrinsic brightness temperature of those clouds is mostly independent of the cloud size; (2) these clouds follow the size-line width relationship ([Larson 1981](#); [Heyer et al. 2009](#)); and (3) the clouds have a similar surface density. Then the molecular gas to CO luminosity relation can be expressed as  $M_{\text{H}_2} = \alpha_{\text{CO}} L'_{\text{CO}}$ , where  $M_{\text{H}_2}$  is defined to include the helium mass, so that  $M_{\text{H}_2} = M_{\text{gas,cloud}}$ , the total gas mass (hence, the virial mass) for molecular clouds ([Solomon & Vanden Bout 2005](#)) and  $\alpha_{\text{CO}}$  is the CO-to- $\text{H}_2$  conversion factor. This is the so-called ‘mist’ model ([Dickman, Snell & Schloerb 1986](#)). Within the Milky Way, the observed relation between virial mass and CO line luminosity for Galactic giant molecular clouds (GMCs; [Solomon et al. 1987](#)) yields  $\alpha_{\text{CO}} \approx 4.6 M_{\odot} (\text{K km s}^{-1} \text{pc}^2)^{-1}$ .

Although the mist model estimates the molecular gas content successfully in the Milky Way, it overestimates the gas mass in more dynamically disrupted systems, such as Ultra Luminous Infrared Galaxies (ULIRGs; [Downes & Solomon 1998](#)). Unlike Galactic clouds or gas distributed in the disk of ‘normal’ galaxies, CO emission maps from ULIRGs show that the molecular gas is contained in dense rotating disks or rings. The CO emission may not come from individual virialized clouds, but from a filled inter-cloud medium, so the line-width is determined by the total dynamical mass ( $M_{\text{dyn}}$ ) in the region (gas and stars). The optically thick CO line emission may trace a medium bound by the gravitational potential around the galactic centre ([Downes, Solomon & Radford 1993](#); [Solomon et al. 1997](#)). In order to estimate the  $M_{\text{H}_2}$  content from  $L'_{\text{CO}}$  in those systems a different approach is required. [Downes & Solomon \(1998\)](#) used kinematic and radiative transfer models to derive  $M_{\text{H}_2}/L'_{\text{CO}}$  ratios in ULIRGs, where most of the CO flux is assumed to come from a warm inter-cloud medium. The models yield  $\alpha_{\text{CO}} \approx 0.8 M_{\odot} (\text{K km s}^{-1} \text{pc}^2)^{-1}$ , a ratio which is roughly six times lower than the standard  $\alpha_{\text{CO}}$  value for the Milky Way. This  $\alpha_{\text{CO}}$  value is usually adopted to estimate the molecular gas content in other non-virialized environments such as galaxy mergers.

On the other hand, from numerical simulations, galaxies that have similar physical conditions have similar CO-to- $\text{H}_2$  factors. This seems to be independent of galaxy morphology or evolutionary state. Thus, rather than bimodal distribution of ‘disk’ and ‘ULIRG’  $\alpha_{\text{CO}}$  values, simulations suggest

that there is a continuum of conversion values that vary with galactic environment (Narayanan et al. 2012).

Therefore, spatially resolved studies of the molecular gas content and its kinematics in galaxies are critical to understand the physical processes that determine the CO-to-H<sub>2</sub> conversion factor and the star formation activity as these two quantities seem to be dependant on the galactic dynamics.

The construction of large samples of intermediate/high-*z* galaxies with direct molecular gas detections (via CO emission) has remained a challenge. Beyond the local Universe, resolved CO detections are limited to the most massive/luminous yet rare galaxies or highly magnified objects (e.g. Saintonge et al. 2013). With ALMA, we are now able to study the physical conditions of the cold molecular gas in ‘typical’ galaxies at these redshifts and test if the actual models successfully explain the characteristics of the intermediate/high-*z* ISM. In this paper, we use state-of-the-art capabilities of ALMA to characterise the CO(*J* = 1 – 0) kinematics of 39 ‘typical’ star-forming/mildly starburst galaxies at  $0.025 < z < 0.32$  drawn from the VALES survey (Villanueva et al. 2017). Combining these ALMA observations to auxiliary data (e.g. Ibar et al. 2015; Hughes et al. 2017a,b), we study how the kinematics of the cold CO(1-0) gas relate to the physical conditions of the ISM. Throughout the paper, we assume a  $\Lambda$ CDM cosmology with  $\Omega_{\Lambda}=0.73$ ,  $\Omega_{\text{m}}=0.27$ , and  $H_0=70 \text{ km s}^{-1} \text{ Mpc}^{-1}$ , implying a spatial resolution, determined by typical major axis of the synthesized beam in the VALES data, of  $3''\text{--}4''$  that corresponds to a physical scale between 2 and 17 kpc.

## 2 SAMPLE SELECTION & OBSERVATIONS

### 2.1 VALES Survey

The VALES sample (Villanueva et al. 2017, hereafter V17) is taken from the *Herschel* Astrophysical TeraHertz Large Area Survey (*H*-ATLAS; Eales et al. 2010; Bourne et al. 2016; Valiante et al. 2016), which is one of the largest infra-red (IR) and submillimetre (submm) surveys covering  $\sim 600 \text{ deg}^2$  of the sky taken by the *Herschel* Space Observatory (Pilbratt et al. 2010). The VALES survey covers a redshift range of  $0.02 < z < 0.35$ , and IR-luminosity range of  $L_{8-1000\mu\text{m}} \approx 10^{10-12} L_{\odot}$ , thus it is an excellent galaxy sample to study the molecular gas dynamics of star-forming and ‘midly’ starburst galaxies at low redshift.

The VALES survey is composed of ALMA observations targeting the CO(1-0) emission line in band 3 for 67 galaxies during Cycle-1 and Cycle-2, from which 49 sources were spectroscopically detected.

We use the V17’s far-infrared (FIR; 8–1000  $\mu\text{m}$ ) luminosities,  $L_{\text{FIR}}$ , which were derived from SEDs constructed with photometry from the Infrared Astronomical Satellite (IRAS; Neugebauer et al. 1984), Wide-field Infrared Survey Explorer (WISE; Wright 2010), and the *Herschel* Photoconductor Array Camera and Spectrometer (PACS; Poglitsch et al. 2010) and the Spectral and Photometric Imaging Receiver (SPIRE; Griffin et al. 2010) instruments. By assuming a Chabrier (2003) initial mass function (IMF), the SFRs are calculated following  $\text{SFR}(M_{\odot} \text{ yr}^{-1}) = 10^{10} \times L_{\text{IR}}(L_{\odot})$  (Kennicutt 1998b). Those values are systematically higher than

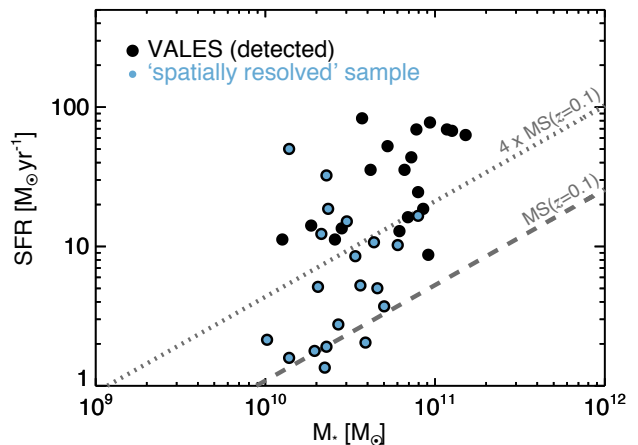


**Figure 1.** The SFR against the  $M_*$  for the 39 galaxies which were spectroscopically detected at  $> 5$ -sigma in datacubes with  $20 \text{ km s}^{-1}$  fixed spectral resolution from the VALES survey (Villanueva et al. 2017). In blue circles we highlight the 20 sources classified as ‘spatially resolved’ (see § 2.1, for more details). The dashed line represents the SFR- $M_*$  relationship for ‘main-sequence’ star-forming galaxies at  $z = 0.1$  following Genzel et al. (2015). The dotted line represents  $4 \times$  the SFR value expected for a ‘main-sequence’ star-forming galaxy at a given stellar mass at  $z = 0.1$ .

the rates estimated from fitting the SEDs with the bayesian code MAGPHYS (da Cunha et al. 2008) by a factor of two. However, the two estimates are well correlated despite this systematic discrepancy (see V17 for more details).

The stellar masses ( $M_*$ ) for our sample were calculated by modelling the SEDs from the photometry provided by the GAMA Panchromatic Data Release (Driver et al. 2016) –in which *all* of our galaxies are present– in 21 bands extending from the far-ultraviolet to far-infrared ( $\sim 0.1 - 500 \mu\text{m}$ ). These observed SEDs have all been modelled with the bayesian SED fitting code MAGPHYS and presented in V17.

The observations, data reduction and analysis are presented in detail for the complete sample in V17, whilst the [CII] luminosity data is presented in Ibar et al. (2015).

The analysis presented in V17 shows ALMA cubes binned at different spectral resolutions (from  $20$  to  $100 \text{ km s}^{-1}$ ) in order to boost the signal to noise (S/N) for spectral detectability. However, the use of low or variable spectral resolution observations to derive and/or analyse galactic kinematics may lead to erroneous conclusions (see § 3.7). Thus, we kept the spectral resolution fixed at  $20 \text{ km s}^{-1}$  despite of the degrade of S/N in order to minimize spectral resolution effects in our dynamical analysis.

Out of the 49 galaxies that were spectroscopically detected in CO(1-0) by V17, we find that only 39 of them are spectroscopically detected at a  $5 \sigma$  significance after fixing the spectral resolution at  $20 \text{ km s}^{-1}$  to all sources. We show these 39 galaxies in the SFR- $M_*$  plane in Fig. 1. Our systems sample the SFRs and stellar masses in the range of  $1 - 84 M_{\odot} \text{ yr}^{-1}$  and  $1 - 15 \times 10^{10} M_{\odot}$ , respectively. We note that the galaxies with high SFR also tend to have high  $M_*$ .

Out of these 39 galaxies, 20 are considered as ‘spatially resolved’ (R) by following these criteria; (1) that the ob-

served CO(1-0) emission extends for more than  $\sqrt{2}$  times the major axis of the synthesized beam; and (2) the observations should have been taken with a projected synthesized beam smaller than 8 kpc. The other 19 sources are classified as ‘compact’ (C). We show the corresponding galaxy classification in the top-right of each CO(1-0) intensity map (Fig. C1). In the forthcoming of this work, in order to guarantee enough independent pixels to be fitted within each galaxy map, we just analyse and model the kinematics of the galaxies considered as ‘resolved’.

To classify our sources as ‘normal’ star-forming or starburst galaxies we use the parametrization defined by Genzel et al. (2015) for the specific star formation rate ( $\text{sSFR} \equiv \text{SFR}/M_*$ ;  $\log[\text{sSFR}(z, M_*)] = -1.12 + 1.14z - 0.19z^2 - (0.3 + 0.13z) \times (\log M_* - 10.5) \text{ Gyr}^{-1}$ ). Galaxies with  $|\text{sSFR}/\text{sSFR}(z, M_*)| \leq 4$  are classified as ‘normal’ star-forming galaxies, whilst all the galaxies with  $\text{sSFR} > 4 \text{ sSFR}(z, M_*)$  are labelled as ‘starburst’. We use the SFR, stellar mass and redshift of each source to perform this classification. In Fig. 1, the dashed line shows the ‘main-sequence’ of star-forming galaxies at  $z = 0.1$ . As an example, the dotted line in Fig. 1 represents our chosen sSFR criterion for galaxies at  $z = 0.1$ .

We also use V17’s morphological classification scheme to assume a bimodal CO-to-H<sub>2</sub> conversion factor of 0.8 or  $4.6 M_\odot (\text{K km s}^{-1} \text{ pc}^2)^{-1}$  depending on whether a galaxy is classified as a ‘merger’ or ‘disk’, respectively. This classification is based on visual inspection of the galaxy images extracted by using the GAMA Panchromatic Swarp Imager tool<sup>1</sup>. We note that in our ‘resolved’ sample, just three galaxies (HATLASJ084630.7+005055, HATLASJ085748.0+004641, HATLASJ090750.0+010141) are classified as ‘mergers’ by the morphological criterion. We do not attempt to perform a kinematic classification of mergers (e.g. Shapiro et al. 2008; Förster Schreiber et al. 2009; Swinbank et al. 2012a; Molina et al. 2017) given that our low spatial resolution tends to smooth the emission and kinematic deviations, making galaxy intensity and velocity fields appear more disky than they actually are (Bellocchi et al. 2012).

The mean molecular gas fraction [ $f_{\text{H}_2} \equiv M_{\text{H}_2}/(M_{\text{H}_2} + M_*)$ ] of the ‘resolved’ sample is 0.22 within a range of 0.06–0.44 with a typical relative error for each measurement of  $\sim 12\%$ .

## 2.2 Galaxy Dynamics

To measure the dynamics of each galaxy, we fit the CO(1-0) emission line ( $v_{\text{rest}} = 115.271 \text{ GHz}$ ) following the approach presented in Swinbank et al. (2012a). We use a  $\chi^2$  minimization procedure, estimating the noise per spectral channel from a surrounding area that does not contain source emission. For a given pixel, we first attempt to identify a CO(1-0) emission line within a squared region that contains the synthesized beam size around that pixel and we take the average spectrum within that region.

Then, we fit a gaussian profile to the spectrum and we impose a S/N > 5 threshold to the best-fit to detect the emission line. If this criterion is not fulfilled, then the squared region around that pixel is increased by one pixel per side

TABLE 1: *K*-band BROADBAND PROPERTIES

ID	$\mu_{0,K}$ mag/'' <sup>2</sup>	$r_{1/2,K}$ ''	$n_S$	PA <sub>K</sub>	$e$ deg	$\chi^2_v$
(1)	(2)	(3)	(4)	(5)	(6)	(7)
HATLASJ083601.5+002617	15.5	5.09	1.93	2.1	0.61	1.09
HATLASJ083745.1-005141	15.5	6.26	2.46	62.8	0.19	0.92
HATLASJ084217.7+021222	12.3	0.63	2.47	168.3	0.22	0.54
HATLASJ084350.7+005535	13.5	1.38	2.61	0.0	0.57	1.12
HATLASJ084428.3+020349	4.2	23.49	8.92	101.1	0.38	1.57
HATLASJ084428.3+020657	15.6	2.04	1.28	58.6	0.77	1.63
HATLASJ084630.7+005055	0.6	0.67	8.44	141.5	0.19	1.05
HATLASJ084907.0-005139	9.7	1.06	4.95	136.4	0.34	1.11
HATLASJ085111.5+013006	11.6	5.20	3.82	114.8	0.77	1.42
HATLASJ085112.9+010342	13.6	2.68	2.82	115.6	0.53	1.16
HATLASJ085340.7+013348	16.9	6.68	2.18	27.4	0.13	1.17
HATLASJ085346.4+001252	14.9	3.31	1.93	46.0	0.77	1.07
HATLASJ085356.5+001256	17.8	4.56	1.56	57.4	0.29	1.08
HATLASJ085450.2+021207	14.0	3.62	2.58	150.3	0.52	1.48
HATLASJ085616.0+005237	13.9	0.97	2.54	78.1	0.10	1.05
HATLASJ085748.0+004641	10.1	0.72	3.48	125.3	0.10	1.28
HATLASJ085828.5+003815	8.8	7.51	5.93	121.0	0.25	1.19
HATLASJ085836.0+013149	–	–	–	–	–	–
HATLASJ090004.9+000447	12.5	1.85	2.84	47.6	0.22	1.47
HATLASJ090750.0+010141	8.2	1.49	5.40	66.3	0.28	1.89
HATLASJ091205.8+002655	9.8	0.97	4.04	52.2	0.07	1.24

**Table 1.** GAMA’s morphological *K*-band photometric parameters for the ‘resolved’ galaxy sub-sample from VALES.  $\mu_{0,K}$  is the central surface brightness value.  $r_{1/2,K}$  and  $n_S$  are the half-light radius and the Sérsic photometric index, respectively. PA<sub>K</sub> is the position angle of the major axis. The ellipticity ‘ $e$ ’ is derived from the semi-major and minor axis ratio ( $e \equiv 1 - b/a$ ). The chi-square of the best two-dimensional fitted photometric model is given in the last column (see §3.1 for more details).

and we search for any emission line again. After this iteration, if the criterion is still not achieved, then we skip to the next pixel.

Considering that we have not applied any spectral filtering for imaging purposes, the fitted line widths correspond to the intrinsic line widths (no deconvolution needed). Nevertheless, in order to consider if an emission line is sufficiently sampled, we only take into account those fits in which the fitted line width is larger than  $\sqrt{2}$  times the channel width ( $\approx 28 \text{ km s}^{-1}$ , e.g. Fig. C1). The spectral resolution is therefore impeding narrower velocity dispersion measurements. We caution that, this masking procedure may lead an overestimated average velocity dispersion value for each galaxy.

<sup>1</sup> <http://gama-psi.icrar.org/psi.php>

TABLE 2: GALAXY PROPERTIES

HATLAS-DR1 ID	RA J2000 (2)	Dec J2000 (3)	$z_{\text{spec}}$ (4)	$\log M_*$ $M_{\odot}$ (5)	$\log L_{\text{FIR}}$ $L_{\odot}$ (6)	$L_{\text{[CII]}}$ $\times 10^8 L_{\odot}$ (7)	$L'_{\text{CO}}$ $\times 10^{10} L_{\odot}$ (8)	$\theta_{\text{WHM}}$ kpc (9)	$r_{1/2\text{CO}}$ kpc (10)	inc. deg (11)	$\sigma_v$ km/s (12)	$V_{\text{rot}}$ km/s (13)	$\chi^2_V$ (14)	Class (15)
HATLASJ083601.5+002617	08:36:01.6	+00:26:18.1	0.03322	10.59±0.1	10.31±0.02	0.97±0.02	0.104±0.004	2.22	3.4±0.1	80.8±0.1	24±2	180±3	0.13	R
HATLASJ083745.1-005141	08:37:45.2	-00:51:40.9	0.03059	10.35±0.1	10.13±0.03	0.73±0.01	0.034±0.003	2.06	4.4±0.3	57.2±0.1	25±1	115±1	0.14	R
HATLASJ083831.9+000045	08:38:31.9	+00:00:45.0	0.07806	10.27±0.1	11.15±0.01	2.43±0.10	0.250±0.019	6.05	—	—	—	—	—	C
HATLASJ084217.7+021222	08:42:17.9	+02:12:23.4	0.09602	10.53±0.1	10.93±0.04	2.28±0.11	0.249±0.020	5.58	12.0±3.1	77.5±0.2	35±7	75±3	0.16	R
HATLASJ084305.0+010858	08:43:05.1	+01:08:56.0	0.07770	10.41±0.2	11.05±0.03	—	0.166±0.017	6.13	—	—	—	—	—	C
HATLASJ084350.7+005535	08:43:50.8	+00:55:34.8	0.07294	10.64±0.1	11.03±0.01	1.70±0.09	0.191±0.016	5.52	4.2±0.3	67.3±0.7	70±8	58±3	0.71	R
HATLASJ084428.3+020349	08:44:28.4	+02:03:49.8	0.02538	10.29±0.1	10.25±0.01	0.33±0.01	0.041±0.003	1.76	2.4±0.4	80.0±0.2	59±14	69±6	0.86	R
HATLASJ084428.3+020657	08:44:28.4	+02:06:57.4	0.07864	10.78±0.1	11.01±0.03	4.51±0.14	0.392±0.051	6.22	6.3±0.5	83.5±0.2	39±2	162±3	2.50	R
HATLASJ084630.7+005055	08:46:30.9	+00:50:53.3	0.13232	10.36±0.1	11.51±0.02	6.22±0.63	0.463±0.042	7.51	4.5±0.5	33.2±0.1	37±28	215±8	20.6	R
HATLASJ084907.0-005139	08:49:07.1	-00:51:37.7	0.06979	10.48±0.1	11.18±0.01	2.28±0.09	0.279±0.022	5.27	4.7±1.3	45.9±0.3	54±3	108±4	0.33	R
HATLASJ085111.5+013006	08:51:11.4	+01:30:06.9	0.05937	10.56±0.1	10.72±0.02	2.66±0.07	0.198±0.007	4.63	6.5±0.4	76.2±0.1	31±8	207±4	0.22	R
HATLASJ085112.9+010342	08:51:12.8	+01:03:43.7	0.02669	10.14±0.1	10.20±0.01	0.24±0.01	0.020±0.003	1.85	1.1±0.3	58.0±0.9	43±19	81±4	0.74	R
HATLASJ085234.4+013419	08:52:33.9	+01:34:22.7	0.19500	10.57±0.1	11.92±0.01	—	1.999±0.012	14.9	—	—	—	—	—	C
HATLASJ085340.7+013348	08:53:40.7	+01:33:47.9	0.04101	10.36±0.1	10.28±0.03	0.95±0.02	0.061±0.003	2.95	3.6±0.3	39.0±0.2	24±3	181±14	0.13	R
HATLASJ085346.3+001252	08:53:46.3	+00:12:52.4	0.05044	10.31±0.1	10.71±0.01	2.18±0.04	0.076±0.002	3.57	6.4±0.4	89.7±0.2	33±5	134±4	0.26	R
HATLASJ085356.3+001256	08:53:56.3	+00:12:56.3	0.05084	10.01±0.1	10.33±0.03	1.41±0.04	0.068±0.002	3.60	2.6±0.2	52.2±0.1	25±4	109±2	0.14	R
HATLASJ085450.2+021207	08:54:50.2	+02:12:08.3	0.05831	10.66±0.1	10.70±0.02	2.30±0.08	0.202±0.019	4.66	3.9±0.1	70.4±0.1	39±16	287±6	1.52	R
HATLASJ085616.0+005237	08:56:16.0	+00:52:36.2	0.16916	10.96±0.1	10.94±0.01	—	0.443±0.076	10.4	—	—	—	—	—	C
HATLASJ085748.0+004641	08:57:48.0	+00:46:38.7	0.07177	10.37±0.1	11.27±0.01	4.69±0.09	0.276±0.014	5.57	4.6±0.3	70.2±0.1	51±5	43±3	0.10	R
HATLASJ085828.5+003815	08:58:28.6	+00:38:14.8	0.05236	10.43±0.1	10.44±0.02	0.94±0.03	0.043±0.005	3.72	2.6±0.2	52.3±0.1	22±2	159±2	0.16	R
HATLASJ085836.0+013149	08:58:36.0	+01:31:49.0	0.10677	10.90±0.1	11.22±0.01	5.30±0.21	0.554±0.011	6.17	11.1±0.8	80.0±0.1	27±4	91±1	0.19	R
HATLASJ090004.9+000447	09:00:05.0	+00:04:46.8	0.05386	10.70±0.1	10.57±0.02	1.86±0.06	0.153±0.022	3.80	2.7±0.1	42.5±0.2	25±2	193±10	0.22	R
HATLASJ090750.0+010141	09:07:50.1	+01:01:41.8	0.12808	10.14±0.1	11.70±0.01	9.33±0.40	0.535±0.045	7.36	10.3±0.6	44.8±1.4	58±6	35±5	0.12	R
HATLASJ090949.6+014847	09:09:49.6	+01:48:46.0	0.18186	10.89±0.1	11.84±0.02	13.8±0.68	1.364±0.093	12.7	—	—	—	—	—	C
HATLASJ091157.2+014453	09:11:57.2	+01:44:53.9	0.16945	10.90±0.2	11.39±0.01	—	0.737±0.072	11.0	—	—	—	—	—	C
HATLASJ091205.8+002655	09:12:05.8	+00:26:55.6	0.05446	10.33±0.1	11.09±0.01	1.45±0.05	0.187±0.011	3.94	2.6±0.3	21.0±0.5	79±24	116±12	0.11	R
HATLASJ091420.0+000509	09:14:20.0	+00:05:10.0	0.20216	10.62±0.1	11.55±0.01	—	0.667±0.114	13.0	—	—	—	—	—	C
HATLASJ091956.9+013852	09:19:57.0	+01:38:51.6	0.17635	10.45±0.1	11.13±0.01	—	0.365±0.048	11.7	—	—	—	—	—	C
HATLASJ113858.4-001629	11:38:58.5	-00:16:30.2	0.16370	10.84±0.1	11.21±0.01	—	0.546±0.129	8.94	—	—	—	—	—	C
HATLASJ114343.9+000203	11:43:44.1	+00:02:02.5	0.18716	10.10±0.1	11.05±0.01	—	0.485±0.089	10.1	—	—	—	—	—	C
HATLASJ114625.0-014511	11:46:25.0	-01:45:13.0	0.16450	10.72±0.1	11.72±0.01	—	0.861±0.084	8.91	—	—	—	—	—	C
HATLASJ121141.8-015730	12:11:41.8	-01:57:29.7	0.31704	11.18±0.1	11.80±0.01	—	0.210	15.1	—	—	—	—	—	C
HATLASJ121253.5-002203	12:12:53.5	-00:22:04.4	0.18548	10.79±0.1	11.11±0.01	—	0.447±0.065	9.71	—	—	—	—	—	C
HATLASJ121427.3+005819	12:14:27.4	+00:58:18.3	0.18045	10.93±0.1	11.27±0.01	—	0.460±0.069	9.63	—	—	—	—	—	C
HATLASJ121446.4-011155	12:14:46.5	-01:11:55.6	0.17971	10.82±0.1	11.55±0.01	—	0.765±0.094	9.45	—	—	—	—	—	C
HATLASJ140912.3-013454	14:09:12.5	-01:34:54.9	0.26492	10.97±0.1	11.89±0.01	—	1.494±0.231	9.17	—	—	—	—	—	C
HATLASJ141008.0+005106	14:10:08.0	+00:51:06.9	0.25641	11.10±0.1	11.83±0.01	—	1.311±0.295	8.80	—	—	—	—	—	C
HATLASJ142057.9+015233	14:20:58.0	+01:52:32.1	0.26462	10.86±0.1	11.64±0.01	—	1.238±0.231	9.55	—	—	—	—	—	C
HATLASJ142517.1+010546	14:25:17.1	+01:05:46.0	0.28069	11.07±0.1	11.84±0.01	—	1.714±0.237	9.98	—	—	—	—	—	C

**Table 2.** Properties of the galaxies with resolved emission from VLES. The FIR luminosities are calculated across the 8–1000  $\mu\text{m}$  wavelength range.  $\theta_{\text{WHM}}$  is the synthesized beam major axis size. The CO(1–0) half-light radii ( $r_{1/2\text{CO}}$ ) are deconvolved by the synthesized beam. The inclination angle is defined as the angle between the line-of-sight (LOS) and the plane perpendicular to the galactic disk (for a face-on galaxy,  $\text{inc} = 0$  deg.).  $\sigma_v$  is the median velocity dispersion corrected for “beam smearing” effects; see §3.6.  $V_{\text{rot}}$  is the rotational velocity at 2 times the CO(1–0) half-light radius corrected for inclination.  $\chi^2_V$  is the reduced chi-square of the best two-dimensional fit. The galaxy classification in the final column denotes ‘Resolved’ (R) or ‘Compact’ (C) (see §2.1 for more details).

### 3 METHODS

#### 3.1 GAMA's morphological models

With the advent of the multiple IFS surveys at high redshift (e.g. Förster Schreiber et al. 2009; Wisnioski 2015; Stott et al. 2016), kinematic models have experienced a rapid development and becoming more complex by taking into account multiple galaxy components and adding multiple degrees of freedom (e.g. Swinbank et al. 2017). The latter increases the parameter degeneracy, especially regarding inclination angle when low spatially resolved observations are analysed. Thus, additional information must be considered in order to derive robust kinematic parameters from the observed velocity fields. With the aim to minimise parameter degeneracy, we supported our kinematic analysis by taking into account previous Sérsic photometry models (Sérsic 1963) available for the GAMA survey data (Table 1; Liske et al. 2015). Those models are produced by using SIGMA (Structural Investigation of Galaxies via Model Analysis; Kelvin et al. 2012) on Sloan Digital Sky Survey (SDSS) and UKIRT Infrared Deep Sky Survey (UKIDSS) imaging data. We use the *K*-band image models to characterise stellar component of each galaxy through the half-light radius ( $r_{1/2,K}$ ), the orientation of major axis indicated by the position angle ( $PA_K$ ), and the inclination angle derived from the minor to major axis ratio ( $b/a$ ). We use this inclination value to constraint the galactic inclination of the molecular gas content in the kinematic modelling. We note, however, that the error estimates produced by SIGMA are determined from the covariance matrix used in the fitting procedure. As a result, the uncertainty of the inclination value tend to be underestimated (Häußler et al. 2007; Bruce et al. 2012). Therefore, we adopt more reasonable error to the galactic inclination and discuss its choice in the following subsection. Out of the 20 resolved galaxies analysed in this work, 19 sources have this morphological GAMA modelling. We do not use the inclination value derived for HATLASJ085836.0+013149 from its morphological model as it implies an unrealistic central surface brightness magnitude value of  $-18 \text{ mag arcsec}^{-2}$ . This galaxy was analysed without constraint on the kinematic parameters.

#### 3.2 Inclination angles

The correct estimate of inclination angles is a critical issue for kinematic analyses. This parameter is used to correct the observed velocity field, which is the projected component of the intrinsic velocity field of the galaxy across the line-of-sight. With the aim to take into account the galactic ‘disk thickness’, we model the galaxies in our sample as oblate spheroid systems. By using the minor-major axis ratio ( $b/a$ ) taken from the GAMA data, the galaxy inclination angle can be expressed as:

$$\cos^2(i) = \frac{(b/a)^2 - q_0^2}{1 - q_0^2}, \quad (1)$$

where ‘ $i$ ’ is the galaxy inclination angle and  $q_0$  is the axis ratio of the galaxy as if it would be seen as an edge-on system (Holmberg 1958). In the thin-disk approximation, i.e.  $q_0 = 0$ , the Equation 1 is reduced to the simplistic approximation ( $b/a$ ) =  $\cos(i)$ . Although we have no information about the

‘disk thickness’ for our sample, we adopt  $q_0 = 0.14$ , which is the mean  $b/a$  ratio found in edge-on disk galaxies at low redshift ( $z < 0.05$ ; Mosenkov et al. 2015). We consider a conservative approach for the inclination angle uncertainties of 10% in order to get realistic error estimates for the inclination angles and use them instead of the underestimated values derived from SIGMA (see 3.1), as suggested by the results of the Monte Carlo methodology used by Epinat et al. (2012). We use the inclination angles derived from SIGMA as initial guesses for our kinematic analysis and we allow them to vary within a  $3\sigma$  range. For the galaxies without a SIGMA fitting, we consider a range between 0 and 90 degrees with an initial guess of ( $b/a$ )  $\sim 0.7$  ( $i \sim 55^\circ$ ), that is the mean axis ratio derived by Law et al. (2012) for a randomly oriented spheroidal galaxy population.

#### 3.3 Kinematic model

We attempt to model the two-dimensional velocity field by first identifying the dynamical centre and the kinematic major axis. Considering the modest spatial resolution of our observations and the smoothness of the intensity maps, we constrain the kinematic centre to the CO(1-0) intensity peak location. We follow Swinbank et al. (2012a) to construct two-dimensional models with an input rotation curve following an arctan function [ $V(r) = \frac{2}{\pi} V_{\text{asym}} \arctan(r/r_t)$ ], where  $V_{\text{asym}}$  is the asymptotic rotational velocity and  $r_t$  is the effective radius at which the rotation curve turns over (Courteau 1997). This model has four free parameters [ $V_{\text{asym}}$ ,  $r_t$ , position angle (PA) and disk inclination] and a genetic algorithm (Charbonneau 1995) is used to find the best fit (see Swinbank et al. 2012a for more details). The parameter uncertainties are calculated by considering a confidence limit of  $\Delta\chi^2_V = 1$ . An example of the best-fit kinematic maps and velocity residuals are shown in Fig. 2, whilst the full sample maps are presented in the appendix (Fig. C1). The best-fit inclination values are given in Table 2. The mean deviation from the best-fit models within the sample (indicated by the typical root-mean-squared; r.m.s) is  $\langle \text{data} - \text{model} \rangle = 17 \pm 9 \text{ km s}^{-1}$  with a range of  $\langle \text{data} - \text{model} \rangle = 7 - 48 \text{ km s}^{-1}$ . We show this value for each galaxy in its residual map.

#### 3.4 CO(1-0) spatial extent

To measure the spatial extent of the molecular gas of each galaxy, we calculate the CO half-light radii ( $r_{1/2,\text{CO}}$ ). These are calculated from the cubes, where the encircled CO(1-0) flux decays to half its total integrated value. The total integrated value is defined as the total CO(1-0) luminosity within a Petrosian radius. We adopted the SDSS Petrosian radius definition with  $R_{P,\text{lim}} = 0.2$ . We account for the ellipticity and position angle of the galaxy obtained from the best-fit disk model. The  $r_{1/2,\text{CO}}$   $1\sigma$  errors are derived by bootstrapping via Monte-Carlo simulations in both, measured emission line intensity and estimated dynamical parameters. The half-light radii are corrected for beam-smearing effects by subtracting the synthesized beam major axis width in quadrature. The median  $r_{1/2,\text{CO}}$  for our sample is  $4.4 \pm 3 \text{ kpc}$  (Table 2).

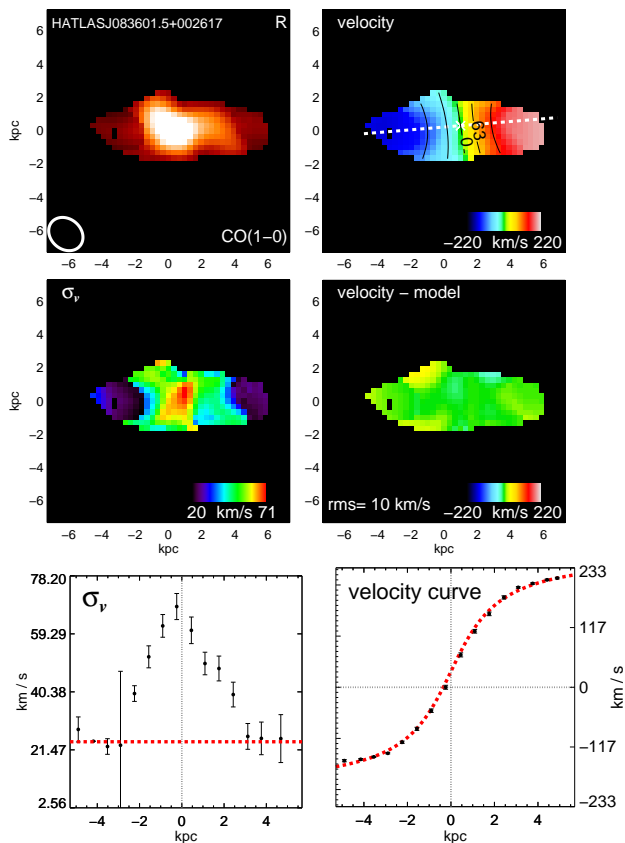


**Figure 2.** Example of the two dimensional maps and one dimensional velocity profiles for one target within our survey. The full sample maps, profiles figures and their explanation are shown in the appendix (Fig. C1). *Left:* From top to bottom; CO(1-0) intensity map, LOS velocity dispersion map and one dimensional velocity dispersion profile. *Right:* From top to bottom; rotational velocity map, residual map, and one dimensional rotational velocity profile.

### 3.5 Rotation Curve & Rotational Velocity

We use the dynamical centre and position angle derived from the best-fit dynamical model to extract the one-dimensional rotation curve across the major kinematic axis of each galaxy. An example of the extracted rotational curves is presented in Fig. 2, whilst the rotational curves for all the sample are shown in the appendix (Fig. C1). We define the rotational velocity corrected for inclination ( $V_{\text{rot}}$ ) as the velocity observed at two half-light radii. We note, however, that we are observing the CO(1-0) emission line, thus the radius at which we are defining the representative rotational velocity of each source may not be directly related to the radius at which, for example, Integral Field Spectroscopy (IFS) surveys might extract rotational velocities using ionized gas dynamics (e.g. Förster Schreiber et al. 2009; Swinbank et al. 2012a; Green et al. 2014; Wisnioski 2015; Stott et al. 2016).

### 3.6 Velocity Gradient Correction & Velocity Dispersion

As a consequence of the modest spatial resolution of our observations compared to the angular extension of the sources, there is a contribution to the derived line widths from the

beam-smearing large-scale velocity motions across the galaxy, which must be corrected for (Davies et al. 2011). This correction is done for each pixel where the CO(1-0) emission is detected. We calculate the luminosity-weighted velocity gradient across the synthesized beam ( $\Delta V/\Delta R$ ) in the model velocity field and we subtract it linearly from the corresponding velocity dispersion value following Eq. A1 from Stott et al. (2016). However, by using this procedure, a  $\sim 20\%$  residuals are expected to remain, especially on the centre of each galaxy where large velocity gradients are expected to be present (Stott et al. 2016).

In order to minimize the residual beam-smearing effects in our sample, we define the global velocity dispersion value ( $\sigma_v$ ) for each galaxy as the median value of the pixels at an angular distance 2 times greater than the angular extension of the synthesized beam from the best-fitted dynamical centre. This procedure usually calculates  $\sigma_v$  by considering 71 pixels on average with a range of 6-256 pixels. In the case of HATLASJ083601.5+002617 we increased the skipped area to 3 times the synthesized beam size as our method failed due to the high galaxy inclination angle ( $\sim 80$  deg.) plus a beam size not large enough to avoid the zone where velocity gradients were contributing to the emission line widths.

While the CO(1-0) emission line width has been traditionally used as a measure of the dynamical mass within a GMC (e.g. Solomon et al. 1987), the synthesized beam size (2-8 kpc) within our sample is larger than the biggest GMC size observed in galaxies ( $\sim 1$  kpc; e.g. Swinbank et al. 2012b); resulting in the smoothness of our galactic intensity maps (Fig. C1). Thus, throughout our work, we interpret the CO(1-0) emission line width as a tracer of the molecular gas random motions seen over a resolution element area. This is the key property of our ‘resolved’ sample as we can study the dynamics of the molecular gas directly. This opens a window of dynamical analyses which is not necessary the same as those performed in IFS galaxy surveys which use (mainly) the ionized gas to characterise the dynamical state of galaxies.

### 3.7 Spatial and spectral resolutions effects

In order to estimate the effect of the spatial and spectral resolution for the VALES sample on the kinematic parameters, we use ALMA Band-3 observations with higher resolution of  $\sim 0''.5$  ( $\sim 1$  kpc scale at  $z \sim 0.1 - 0.2$ ) and  $12 \text{ km s}^{-1}$  towards three VALES galaxies (Ibar et al. in prep.). The high resolution of those observations allows us to study in detail how spectral resolution and beam-smearing effects affect the derived kinematic parameters.

We create mock-observations by spatially degrading the images using two-dimensional Gaussian kernel, while also re-binning the spectral channels to mimic lower spectral resolutions. The channel width is increased by  $12 \text{ km s}^{-1}$  per step between  $\sim 12 - 84 \text{ km s}^{-1}$ , whilst the spatial resolution is degraded by 1 kpc per step between  $\sim 1 - 7$  kpc (up to  $\sim 3$  times the ‘fiducial’ half-light radius). From those mock data-cubes we fit the CO(1-0) emission line, we derive its best-fit kinematic model and calculate the  $V_{\text{rot}}$ ,  $\sigma_v$  and  $r_{1/2, \text{CO}}$  following the procedures described in the previous sections, but we keep the position angle fixed to the value obtained for the data-cube with higher spatial and spectral resolutions. In

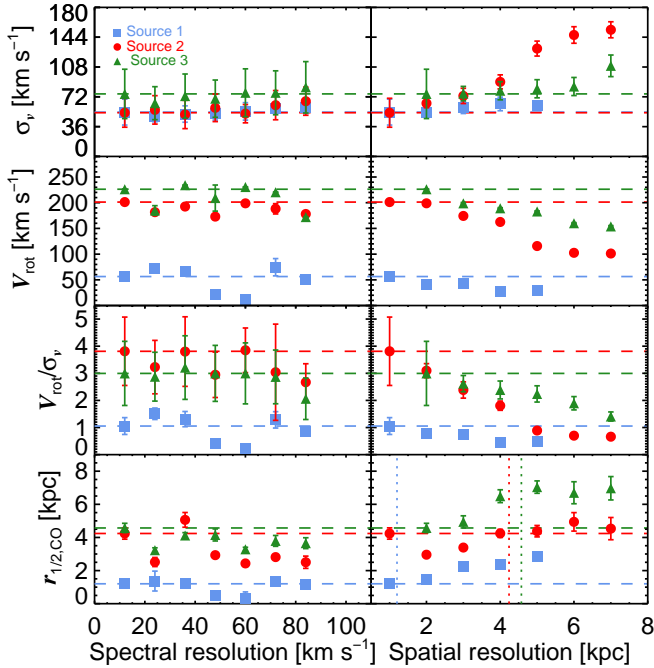


**Figure 3.** Velocity dispersion, rotational velocity, rotational velocity to velocity dispersion ratio ( $V_{\text{rot}}/\sigma_v$ ) and CO(1-0) intensity half-light radius (rows) as a function of the spectral and spatial resolution (columns). Those values were derived from mock data-cubes produced by the convolution of a three dimensional gaussian kernel with the original observations. The spatial resolution corresponds to the projected major axis (FWHM) of the synthesized beam. The blue, red and green horizontal dashed lines represent the kinematic ‘fiducial’ values for each source. The blue, red and green vertical dotted lines represent the ‘fiducial’  $r_{1/2,\text{CO}}$  values for each galaxy (see § 3.7 for more details).

Fig. 3 we show how the fitted kinematic parameters (rows) depend on spectral resolution (left column) at fixed  $\sim 1$  kpc scale and spatial resolution (right column) at fixed  $12 \text{ km s}^{-1}$  for the three sources. We consider the ‘fiducial’ value of each kinematic parameter for each source as the values derived for the data-cubes with higher spectral and spatial resolutions ( $12 \text{ km s}^{-1}$  and  $\sim 1$  kpc), and are represented by the horizontal dashed lines in each plot. The fiducial values for the three galaxies are;  $V_{\text{rot}} = 56, 200$  and  $226 \text{ km s}^{-1}$ ;  $\sigma_v = 54, 53$  and  $76 \text{ km s}^{-1}$ ; and  $r_{1/2,\text{CO}} = 1.2, 4.2$  and  $4.6$  kpc.

In Fig. 3, we see how the measured galactic velocity dispersion remains constant when the spectral resolution is degraded. We also see an increase of the velocity dispersion when we spatially degrade the cubes, however, we note that the galaxy with the lowest ‘fiducial’ rotational velocity value is also the galaxy less affected by spatial resolution effect. This is consistent with the picture in which the velocity gradient within the beam area contributes to the emission line width represented by the velocity dispersion. We note also that galaxy mass and inclination may also affect the  $\sigma_v$  estimation (e.g. Burkert et al. 2016).

In the second row of Fig. 3 we measure  $V_{\text{rot}}$  for each data-cube. Although we can recover nearly the same  $V_{\text{rot}}$  value regardless of the spectral resolution, we can see how it varies when we spatially degrade the cubes. At poor spa-

tial resolution, lower rotational velocity values are recovered. This effect is expected as the observed emission line is the result of the convolution of the emission lines produced within the beam area. This convolution favour brighter emission lines which are mainly produced in the central part of the galaxy where  $V_{\text{rot}}$  is lower.

In the third row of Fig. 3 we show the variation of the  $V_{\text{rot}}/\sigma_v$  ratio as a function of spectral and spatial resolutions. We see how this ratio is not affected by the increase of the channel width. However, we observe a decrease of the  $V_{\text{rot}}/\sigma_v$  ratio with lower spatial resolution. This is produced by a combination of both effects, the underestimation and overestimation of the  $V_{\text{rot}}$  and  $\sigma_v$  values, respectively. However the way in which the  $V_{\text{rot}}/\sigma_v$  ratio decreases seems to be different for each target, suggesting that the internal kinematics of each galaxy may affect the derived  $V_{\text{rot}}/\sigma_v$  ratio through the convolution with the synthesized beam.

In the four row of Fig. 3 we see how  $r_{1/2,\text{CO}}$  does not vary significantly with spectral resolution in any source. The gain of flux from the outskirts of each target seems to be marginal compared to the total flux of the source. On the other hand, we see a clear increase of  $r_{1/2,\text{CO}}$  when we lower the spatial resolution. We note that the derived half-light radii tend to suffer an appreciable increase of their value when the synthesized beam size becomes comparable to the ‘fiducial’  $r_{1/2,\text{CO}}$  value for each galaxy (dotted vertical lines).

As a summary, the velocity dispersion and half-light radius parameters seem to be saturated to a minimum value limited by the spatial resolution. The  $V_{\text{rot}}/\sigma_v$  ratio tend to decrease towards low spatial resolution. However, dispersion dominated sources seem to be less affected by this effect. Thus, high spatial resolution data is required to obtain reliable estimates of those parameters. We find no trend between the spectral resolution and the kinematic estimates from our observations.

Taking into account the resolution effects discussed above, we set the spectral resolution to  $20 \text{ km s}^{-1}$ , the maximum spectral resolution possible for our observations. We expect that spectral resolution effects do not strongly influence the conclusions of our work. We set this spectral resolution regardless of the spatial resolution effects inherent in our observations which may imply an overestimation of the observed  $\sigma_v$  and  $r_{1/2,\text{CO}}$  values and an underestimation of the  $V_{\text{rot}}$  value for our sources.

## 4 RESULTS & DISCUSSION

### 4.1 Morphological and kinematic properties

We show the CO(1-0) intensity, velocity and line of sight velocity dispersion maps for our sample in the appendix (Fig. C1). The intensity maps show smooth distributions of emission with no level of clumpiness except for HATLASJ085340.7+013348 source. Despite the low resolution data, most of our sources show a rotational pattern in their velocity maps (Fig. C1), with the larger rotational velocity values being preferentially measured in galaxies at lower  $z$ . We note that this bias effect may be mainly produced by the IR flux selection criteria used within the VALES sample (see § 2.1). In particular, for our resolved sample, the flux criterion selects  $0.02 < z < 0.2$  ‘normal’ star-forming ro-



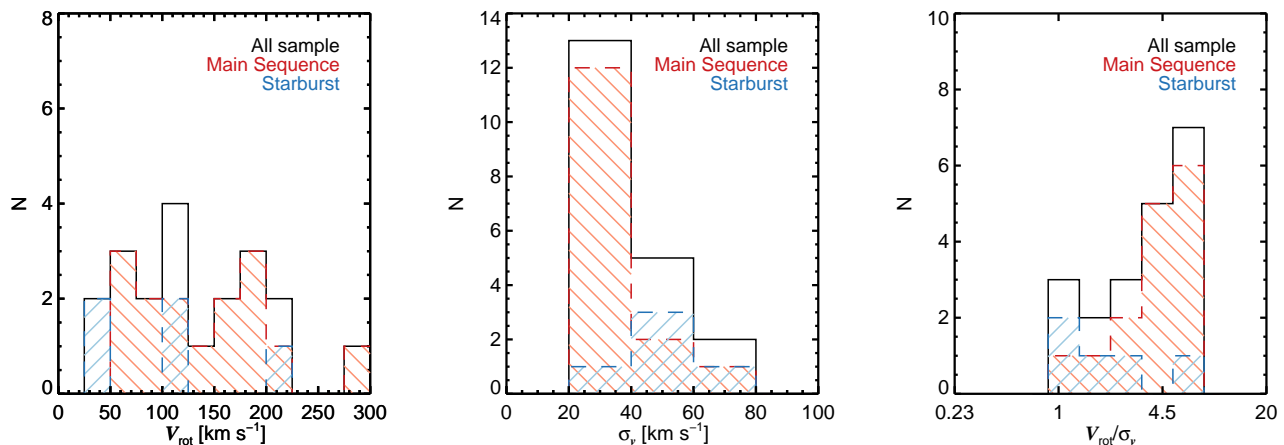


**Figure 4.** The distribution of the rotational velocity ( $V_{\text{rot}}$ ; *Left*), velocity dispersion ( $\sigma_v$ ; *middle*) and  $V_{\text{rot}}/\sigma_v$  (*Right*) within our sample. In the three panels we also show the distributions for the ‘normal’ star-forming galaxies (dashed-red) and ‘starburst’ galaxies (dashed-blue). This classification was done by following the same procedure done by V17 for the VALES survey (see § 2.1). Our resolved sample shows a wide ride of rotation velocities and velocity dispersions.

tating disk-like galaxies, whilst it also selects  $0.1 < z < 0.35$  starburst galaxies with high velocity dispersion (Table 2).

We note that we find a median  $r_{1/2,K}/r_{1/2,\text{CO}}$  ratio of  $\sim 1$ , i.e., the molecular gas component shows an spatial extension comparable to stellar component in our galaxies. This is consistent with molecular gas observations of galaxies in the local universe (e.g. Bolatto et al. 2017). We note that the  $r_{1/2,K}/r_{1/2,\text{CO}}$  median ratio is lower than the median value ( $\sim 1.6$ ) reported by V17 for the VALES sample. We note that this difference could be explained by considering that our emission line fitting routine is able to find CO emission at larger radius than the V17’s procedure. Nevertheless, we calculate the CO and  $K$ -band half-light radius by taking into account the projection effects (i.e. galactic PA and inclination angles), whilst V17 do not consider for such effects.

In Fig. 4 we show the distribution of  $V_{\text{rot}}$ ,  $\sigma_v$ , and the  $V_{\text{rot}}/\sigma_v$  ratio for our resolved sample. The  $V_{\text{rot}}$  values ranges from 35–287  $\text{km s}^{-1}$ . The starburst and ‘normal’ star-forming galaxies show rotational velocities across the full range of the  $V_{\text{rot}}$  distribution. The velocity dispersion values ranges from 22–79  $\text{km s}^{-1}$ . We find median velocity dispersion values of 31 and 53  $\text{km s}^{-1}$  for the ‘normal’ star-forming and starburst galaxies, respectively. However, the  $\sigma_v$  values are susceptible to the procedure used to estimate them. Different methods can lead inconsistent results even when the same sample is analysed (e.g. Stott et al. 2016). Thus, we perform the method developed by Wisnioski (2015) to calculate the velocity dispersion values ( $\sigma_{v,W}$ ) in our sample and to compare with our  $\sigma_v$  values. This method calculates the velocity dispersion values across the major axis of the galaxy, but far from the galactic centre where velocity gradients contribute to the observed line widths (see Wisnioski 2015, for more details).

We found a median  $\sigma_{v,W}$  value of 36  $\text{km s}^{-1}$ , and  $\sigma_{v,W}$  ranges between 19–70  $\text{km s}^{-1}$ . This median value is in agreement with the median  $\sigma_v$  value (37  $\text{km s}^{-1}$ ) derived by our procedure. The derived velocity dispersion ranges are also consistent for both methods. Thus, the slightly overestimation of the  $\sigma_v$  values produced by our procedure should not change the results presented in our work. We caution that

we can not neglect overestimation of the velocity dispersion values produced by spatial resolution effects from this analysis.

The  $V_{\text{rot}}/\sigma_v$  ratio range between 0.6–7.5, with the starburst galaxies preferentially to showing the lower values. The median  $V_{\text{rot}}/\sigma_v$  ratio for our sample is 4.1, and the median  $V_{\text{rot}}/\sigma_v$  values for the ‘normal’ star-forming and starburst sub-samples are 4.3 and 1.6, respectively. Our sample shows a large variety of  $V_{\text{rot}}/\sigma_v$  ratios, from high values comparable to local thin disk galaxies ( $V/\sigma_v \sim 10 - 20$  Epinat et al. 2010; Bershadly 2010), to low values comparable to the  $V_{\text{rot}}/\sigma_v$  ratios observed in  $z \sim 1$  systems (e.g.  $V/\sigma_v \sim 2 - 5$  Förster Schreiber et al. 2009; Wisnioski 2015; Stott et al. 2016).

In Fig. 5 we study the evolution of the  $V_{\text{rot}}/\sigma_v$  ratio at  $z = 0.10 - 1.0$ . We compare with the median  $V_{\text{rot}}/\sigma_v$  values estimated for the GHASP (Epinat et al. 2010), CARMA-EDGE (Bolatto et al. 2017), DYNAMO (Green et al. 2014), KMOS3D (Wisnioski 2015), and KROSS (Stott et al. 2016) surveys. The continuous line and the grey-shaded area represent the best-fit relation and the  $1\sigma$  region estimated from the DEEP2 survey (Kassin et al. 2012) at  $z = 0.2 - 1.0$ , respectively. The dashed line represent an extrapolation of this relation at low- $z$ . DEEP2 is the only long-slit survey considered in Fig. 5. We just consider the galaxies with stellar masses between  $M_* = 10^{10-11} M_{\odot}$ , approximately the same stellar mass range covered by our sample (see Fig. 1). We also plot the median  $V_{\text{rot}}/\sigma_v$  values for the galaxies classified as ‘starburst’ and ‘normal’ galaxies within our sample and the DYNAMO sample as both surveys study star-forming galaxies the same epoch. However, the DYNAMO SFRs are based on dust-corrected  $H\alpha$  emission line measurements, whilst the SFR estimates for our sample are estimated by applying SED fitting. We also note that our sample and the CARMA-EDGE survey observe molecular gas kinematics, whilst GHASP, DYNAMO, KMOS3D and KROSS surveys study ionized gas kinematics.

The median  $V_{\text{rot}}/\sigma_v$  value for our sample is slightly lower but still consistent with the expected value at  $z \sim 0.06$ . This value is also comparable with the median value found for

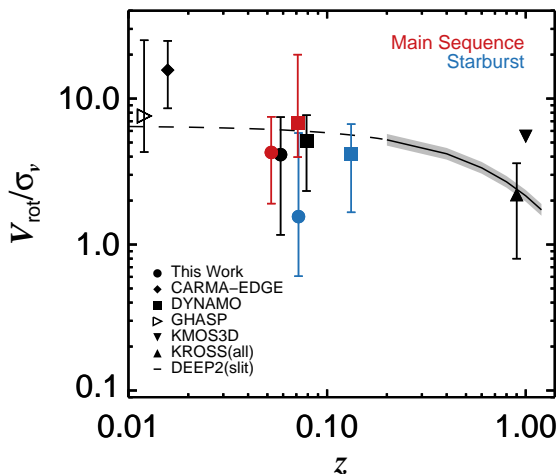


**Figure 5.** Evolution of the  $V_{\text{rot}}/\sigma_v$  ratio at  $z \approx 0.01 - 1.0$ . The symbols represent the median values for each survey and the error bars correspond to the  $1\sigma$  region calculated from the 16th and 84th percentiles for each population. The CARMA-EDGE kinetic data are extracted by using the same procedure explained in previous sections but assuming thin disk geometry (see Appendix B, for more details). We classify our sources and the DYNAMO galaxies as ‘starburst’ or ‘normal’ star-forming galaxy following the same procedure done by V17 for the VALES survey (see § 2.1). The KMOS3D data correspond to the median value for ‘main sequence’ rotationally supported star-forming disk galaxies at  $z \sim 1$ , whilst the KROSS data correspond to the median value for all sample, i.e., including ‘main sequence’ dispersion dominated galaxies. The black line and the shaded area represent the best-fit and  $1\sigma$  region measured for the single slit DEEP2 survey. The dashed line represents the extrapolation of the best-fit to the DEEP2 survey data to lower redshifts

the KMOS3D sample of ‘main-sequence’ rotating disks star-forming galaxies at  $z \sim 1$ . However, the median  $V_{\text{rot}}/\sigma_v$  value of our survey is highly influenced by the low  $V_{\text{rot}}/\sigma_v$  ratios measured for our starburst galaxies (Fig 4). If we do not consider those starburst systems, we find that the median  $V_{\text{rot}}/\sigma_v$  value for the ‘normal’ star-forming galaxies in our sample is consistent with the expected value for local galaxies. It is also consistent with the median  $V_{\text{rot}}/\sigma_v$  value measured for ‘normal’ star-forming galaxies within the DYNAMO survey at nearly the same epoch.

Nevertheless, the median  $V_{\text{rot}}/\sigma_v$  for our starburst galaxies is  $\sim 2.7\times$  lower than the median value observed for the DYNAMO starburst galaxies at the same redshift. Although both values are consistent within  $1\sigma$  error. A difference between the spatial extension of the ionized gas compared to the molecular gas across the galaxy may explain this discrepancy. An extended ionized gas component would allow to measure  $V_{\text{rot}}$  in the flat part of the rotation curve whilst the molecular gas observations would not allow to do it (e.g. HATLASJ084217.7+021222). On the other hand, different procedures used to calculate  $\sigma_v$  may also explain this discrepancy. However, the different spatial resolution at which both surveys were made is likely to be producing the discrepancy between both  $V_{\text{rot}}/\sigma_v$  ratios. The DYNAMO galaxies were observed in natural seeing conditions ( $\theta_{\text{FWHM}} = 0''.9 - 4''$ ), whilst our sample was observed at  $\theta_{\text{FWHM}} = 3'' - 4''$ .

Regardless of the discrepancy of the median  $V_{\text{rot}}/\sigma_v$  measured for our sample and the DYNAMO survey, Fig 5 show that starburst galaxies at  $z \sim 0.1 - 0.2$  present typical  $V_{\text{rot}}/\sigma_v$  which are consistent with median the  $V_{\text{rot}}/\sigma_v$  values presented for the KMOS3D and KROSS surveys at  $z \sim 1$  (Wisnioski 2015; Stott et al. 2016). However, high spatial resolution observations of a large sample of the low- $z$  starburst galaxies is needed to test this result.

## 4.2 Luminosity dependence on galactic kinematics

### 4.2.1 CO(1-0) luminosity

The CO(1-0) luminosity has been widely used as an estimator of the  $\text{H}_2$  mass (Bolatto et al. 2013). Through a dynamically calibrated CO-to- $\text{H}_2$  conversion factor, reliable molecular mass estimates can be achieved (e.g. Solomon et al. 1987; Downes & Solomon 1998). Thus, depending on the dynamical model, we may expect some dependence of the CO luminosity on the galactic dynamics.

In the top panel of Fig. 6 we show the galactic  $L'_{\text{CO}}$  as a function of the rotational velocity to dispersion velocity ratio ( $V_{\text{rot}}/\sigma_v$ ). The Spearman’s rank correlation coefficient ( $\rho_{\text{Spearman}}$ ) is  $-0.23$  with a probability of 32% that the correlation is produced by chance. Thus, we find a tentative weak correlation between  $L'_{\text{CO}}$  and  $V_{\text{rot}}/\sigma_v$ . in our data, suggesting that the CO luminosity might tend to decrease at higher  $V_{\text{rot}}/\sigma_v$ . Considering that  $V_{\text{rot}}/\sigma_v$  measures the level of support given by ordered versus disordered motion support within a galaxy, then we suggest that turbulence supported galaxies tend to have greater  $L'_{\text{CO}}$ .

The high  $L'_{\text{CO}}$  values may reflect high molecular gas masses in systems with low  $V_{\text{rot}}/\sigma_v$  values. On the other hand, we may also expect that systems with high SFRs produce more UV photons which heats the gas through the photoelectric effect on dust grains. This change of gas temperature may also affect the CO-to- $\text{H}_2$  conversion factor (Bolatto et al. 2013). However, we lack of the adequate observations to test this.

We also note that low  $V_{\text{rot}}/\sigma_v$  ratios can be present in both, disk-like galaxies and major-merger systems (Molina et al. 2017), thus, the weak correlation found in Fig. 6 suggests that the increase of the CO(1-0) luminosity may not be associated only to major merger events in agreement with previous results from numerical simulations (Shetty et al. 2011b; Narayanan et al. 2012; Papadopoulos et al. 2012). This weak correlation also suggests that turbulence may play a role in the enhancement of  $L'_{\text{CO}}$  in galaxies. Nevertheless, higher spatial resolution CO(1-0) observations are required to properly discard or validate the possible trend between CO(1-0) luminosity and  $V_{\text{rot}}/\sigma_v$ .

### 4.2.2 [C II] luminosity

The [C II]  $\lambda 157.74 \mu\text{m}$  emission line ( $\nu_{\text{rest}} = 1900.54 \text{ GHz}$ ) is a far-infrared fine-structure line with a low ionization potential (11.26 eV) that makes it a key participant in the cooling of the warm and diffuse ISM to the cold and dense clouds (Dalgarno & McCray 1972). This emission line is a tracer of all the different stages of evolution of the ISM and detailed characterisation of its emergence has been made for the Milky Way and local galaxies (e.g. Kramer et al. 2013;

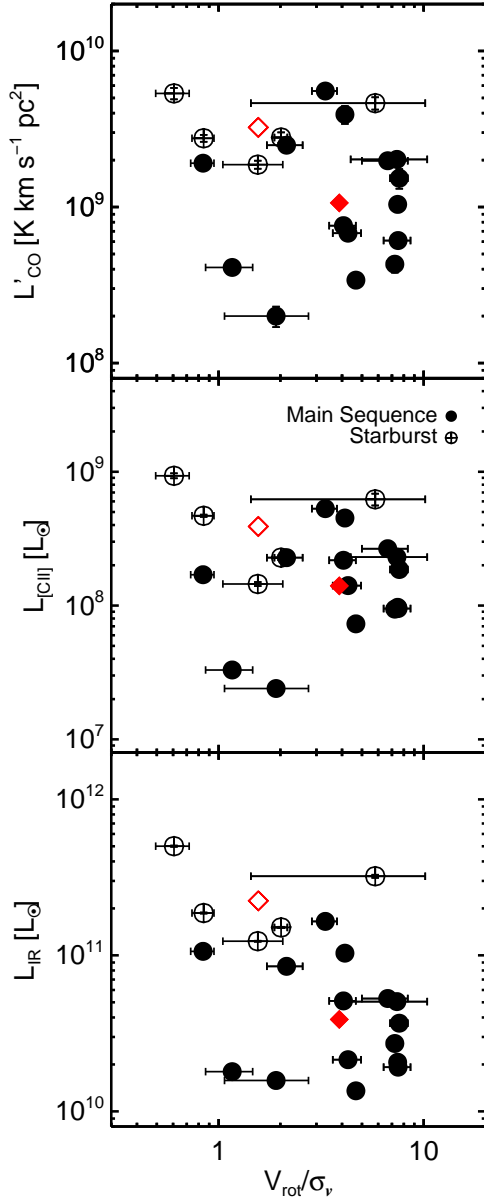


**Figure 6.** From top to bottom: CO(1-0), [C II] and IR luminosities as a function of the  $V_{\text{rot}}/\sigma_v$  ratio for our sample. We also classify the sources as ‘starburst’ or ‘normal’ star-forming galaxy. The red open and filled diamonds represent the mean value (in log-space) for the ‘starburst’ and ‘normal’ star-forming galaxies respectively in each panel. We a tentative anti-correlation between the  $L_{\text{IR}}$  luminosity and the  $V_{\text{rot}}/\sigma_v$ . Galaxies with greater pressure support, reflected by the low  $V_{\text{rot}}/\sigma_v$  ratio, tend to show higher CO(1-0), [C II] and  $L_{\text{IR}}$  luminosities. The tentative anti-correlations may suggest a smooth transition between ‘starburst’ and ‘normal’ star-forming galaxies within our VALES sample.

Pineda et al. 2013; Pineda, Langer & Goldsmith 2014) suggesting that different ISM phases produce roughly comparable contributions to the [C II] luminosity (Madden et al. 1993). However, such detailed characterisations are impeded by observational limitations in distant galaxies which are typically detected in a single telescope beam. Thus, the [C II] line intensity is related to an average quantity that arises

from a mix of the ISM phases (e.g. Gullberg et al. 2015, and references therein). Nevertheless, physical properties of the gaseous components of the ISM may be characterised by studying correlations between the [C II] emission with various galaxy properties [e.g. CO(1-0),  $L_{\text{IR}}$ ; Ibar et al. 2015; Hughes et al. 2017a].

In the middle panel of Fig 6 we show the [C II] luminosity as a function of the  $V_{\text{rot}}/\sigma_v$  ratio for our galaxies. We find a weak correlation between these two quantities. We measure a  $\rho_{\text{Spearman}} = -0.16$  with a probability of 50% that the correlation is produced by chance. This may indicate that galaxies with lower  $V_{\text{rot}}/\sigma_v$  values have higher [C II] luminosity. However, we do not attempt to fit the data as we just have two galaxies measured [C II] luminosity at  $L_{[\text{CII}]} < 7 \times 10^7 L_{\odot}$ . We need more [C II] luminosity measurements, especially at  $L_{[\text{CII}]} < 7 \times 10^7 L_{\odot}$ , in order to discard or validate the possible trend between [C II] luminosity and  $V_{\text{rot}}/\sigma_v$ . [C II] spatially resolved observations would be also useful in order to account for extended and/or nuclear emission effects (e.g. Díaz-Santos et al. 2014).

#### 4.2.3 IR luminosity & the $L_{[\text{CII}]} / L_{\text{IR}}$ deficit

Infrared luminosities are commonly used as a tracer of the star formation activity in galaxies. It can be understood as the emitted UV radiation from young stars which is re-processed by dust. In the limit of complete obscuration the re-emitted  $L_{\text{IR}}$  will effectively provide a bolometric measure of the SFR (Kennicutt 1998a). However, if the attenuation of the stellar light is not completely re-processed, then the IR emission may underestimate the SFR. Applying SED fitting methods, the IR emission can be also used as a tracer of dust temperature ( $T_{\text{dust}}$ ) and mass ( $M_{\text{dust}}$ ; e.g. Draine & Li 2007; Ibar et al. 2015).

In the bottom panel of Fig 6 we show the  $L_{\text{IR}}$  compared to the  $V_{\text{rot}}/\sigma_v$  ratio for our sources. The data present an anti-correlation with  $\rho_{\text{Spearman}} = -0.44$  with a probability of 5% that the correlation is produced by chance. Sources with greater  $L_{\text{IR}}$  have lower  $V_{\text{rot}}/\sigma_v$  values, indicating that high IR-luminosities are likely to be present in systems where pressure support becomes comparable and even greater than rotational support. We note that  $L_{\text{IR}}$  show strong anti-correlation with the  $V_{\text{rot}}/\sigma_v$  ratio than the CO luminosity. This suggests that the  $L_{\text{IR}}/L'_{\text{CO}}$  ratio correlates with the  $V_{\text{rot}}/\sigma_v$  values. We will discuss this further in § 4.7.

The IR luminosity has also been traditionally compared to the [C II] luminosity (e.g. Stacey et al. 1991). The [C II] luminosity to IR luminosity ratio ( $L_{[\text{CII}]} / L_{\text{IR}}$ ) is found to be roughly constant for local star-forming galaxies with  $L_{\text{IR}} < 10^{11} L_{\odot}$ , but decreases at higher luminosities (e.g. Stacey et al. 1991; Malhotra et al. 1997). This is the so-called ‘[C II] deficit’. However, the intricate decomposition of the [C II] emission into the different ISM phases complicates the interpretation of this correlation (e.g. Ibar et al. 2015). Therefore, additional comparisons with other galactic properties are needed. Considering that our ‘resolved’ VALES sample covers the  $10^{10-12} L_{\odot}$  IR luminosity range, it is an ideal sample to study the ‘[C II] deficit’ from a kinematic point of view.

In Fig. 7 we show the  $L_{[\text{CII}]} / L_{\text{IR}}$  as a function of the  $V_{\text{rot}}/\sigma_v$  ratio. We find that  $L_{[\text{CII}]} / L_{\text{IR}}$  increases at high  $V_{\text{rot}}/\sigma_v$

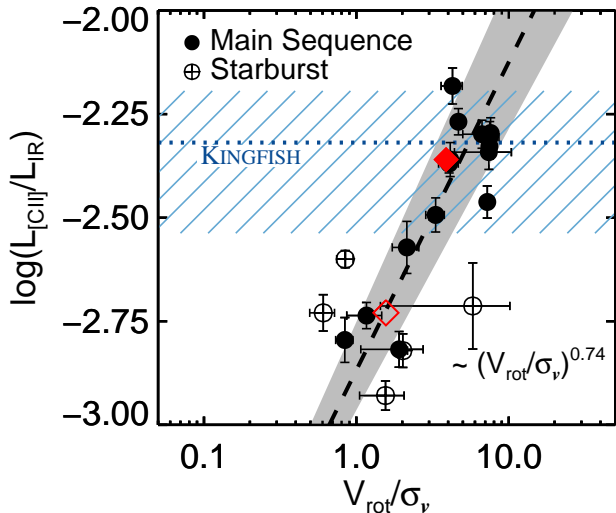


**Figure 7.**  $L_{[\text{CII}]} / L_{\text{IR}}$  ratio as a function of the  $V_{\text{rot}} / \sigma_v$  ratio for our sample. We also classify the sources as ‘starburst’ or ‘normal’ star-forming galaxy. The dashed line represents the best power-law fit to the data and the grey-shaded area represents its  $1\sigma$  error. The best-fit slope is presented in the plot. The red open and filled diamond represent the mean value (in log-space) for the ‘starburst’ and ‘normal’ star-forming galaxies, respectively. The horizontal dotted blue line and the blue-dashed area represent the median  $L_{[\text{CII}]} / L_{\text{IR}}$  ratio and its  $1\sigma$  region for the KINGFISH survey data regardless of the kinematics, respectively (Smith et al. 2017). We find an increase of the  $[\text{CII}] / \text{IR}$  ratio when the  $V_{\text{rot}} / \sigma_v$  ratio increases.

ratios, but shows a significant scatter at low  $V_{\text{rot}} / \sigma_v$  values. This correlation has  $\rho_{\text{Spearman}} = 0.76$  with a probability of 0.0001% that the correlation is produced by chance. We note that this probability is significantly lower than the  $L_{[\text{CII}]} - V_{\text{rot}} / \sigma_v$  and  $L_{\text{IR}} - V_{\text{rot}} / \sigma_v$  Spearman correlation’s probabilities. The data are well-represented by a power-law with best-fit slope of  $0.74 \pm 0.14$ . Considering that a high  $V_{\text{rot}} / \sigma_v$  value suggests a host galaxy with a dominant disk geometry, then our finding is consistent with Ibar et al. (2015), who found that galaxies presenting a prominent disk show higher  $L_{[\text{CII}]} / L_{\text{IR}}$  ratios than those that do not present disk morphologies.

In Fig. 7 we also compare our measured  $L_{[\text{CII}]} / L_{\text{IR}}$  ratios with the values derived for the Key Insights on Nearby Galaxies—a Far-Infrared Survey with *Herschel* (KINGFISH; Kennicutt et al. 2011). These  $L_{[\text{CII}]} / L_{\text{IR}}$  ratios are measured from over  $\sim 15000$  resolved regions within 54 nearby ( $d \leq 30$  Mpc) galaxies (Smith et al. 2017) and we represent the median  $L_{[\text{CII}]} / L_{\text{IR}}$  ratio of the sample and its  $1\sigma$  region with the dotted blue line and the blue dashed-area, respectively. A sub-sample of eight galaxies from the KINGFISH survey have measured molecular gas dynamics from the HERA CO Line Emission Survey (HERACLES; Leroy et al. 2009; Mogotsi et al. 2016), and accurate rotation curves derived through H I observations from The H I Nearby Galaxy Survey (THINGS; Walter et al. 2008; de Blok et al. 2008). Those observations suggest  $V_{\text{rot}} / \sigma_v \gtrsim 10$  for this sub-sample. However, as we can not assume that this sub-sample is repre-

sentative from the complete survey, we do not assume any constraint in the  $V_{\text{rot}} / \sigma_v$  ratio for the KINGFISH data.

We find that the VALES galaxies with  $V_{\text{rot}} / \sigma_v \gtrsim 3$  present similar  $L_{[\text{CII}]} / L_{\text{IR}}$  ratios compared to the KINGFISH data. However, the VALES galaxies with  $V_{\text{rot}} / \sigma_v \lesssim 3$  tend to show even lower  $L_{[\text{CII}]} / L_{\text{IR}}$  values. This is independent whether the galaxy was classified as ‘normal’ star-forming galaxy or ‘starburst’.

We note that our sample is not significantly contaminated by AGNs (V17) and the  $[\text{CII}]$  emission is likely to be optically thin within the galaxies of our sample as based on photodissociation region (PDR) modelling (Hughes et al. 2017a), suggesting that these two possible effects are not substantially affecting the trend observed in Fig. 7. An increase of the star formation efficiency seems not to produce the trend seen between the  $L_{[\text{CII}]} / L_{\text{IR}}$  ratio with the  $V_{\text{rot}} / \sigma_v$  ratio, as most of the galaxies shown in the bottom panel of Fig. 6 form stars at apparently the same efficiency (V17).

### 4.3 PDR modelling & molecular gas kinematics

PDR modelling has been traditionally used to derive the physical properties of the gaseous components of the ISM (e.g. Tielens & Hollenbach 1985). Although each PDR code has its own unique model setup and output, it usually determines the physical parameters by solving chemical and energy balance while also solving the respective radiative transfer equations (Röllig et al. 2007).

For the VALES survey, Hughes et al. (2017a) applied the PDR model of Kaufman et al. (1999, 2006), which is an updated version of the PDR model of Tielens & Hollenbach (1985). The model treats PDR regions as homogeneous infinite plane slabs of hydrogen with physical conditions characterised by the hydrogen nuclei density ( $n_H$ ) and the strength of the incident FUV radiation field,  $G_0$ , which is normalised to the Habing Field (Habing 1968). The model covers a density range of  $10 < n_H < 10^7 \text{ cm}^{-3}$  and FUV radiation field strength range of  $10^{0.5} < G_0 < 10^{6.5}$ . In this model, the gas is assumed to be collisionally heated via the ejection of photoelectrons from dust grains and polycyclic aromatic hydrocarbon (PAH) molecules by FUV photons, and gas cooling from line emission is predicted by simultaneously solving the chemical and energy equilibrium in the slab.

Hughes et al. (2017a) assumed that the galactic emission comes from a single PDR. They compare the predicted  $L_{[\text{CII}]} / L_{\text{IR}}$  and  $L'_{\text{CO}} / L_{\text{IR}}$  luminosity ratios with the observed quantities. However, since the fragment of the  $[\text{CII}]$  emission produced in PDRs with respect to the total galactic emission is observed to vary between 0.5–0.7 (e.g. Stacey et al. 1991; Malhotra et al. 2001; Oberst et al. 2006; Stacey et al. 2010a). They also consider two additional models in which they adjust the parameters to match to the 50% and 70% values of the total  $[\text{CII}]$  luminosity for each galaxy. In these two models, they also consider the missing CO(1-0) flux emitted along different line-of-sight by multiplying their observed CO(1-0) emission by a factor of two (see Hughes et al. 2017a for more details). Although these assumptions can modify the values of the derived PDR parameters, in the remaining analysis we will only consider the possible trends seen between  $n_H$  and  $G_0$  with respect to the molecular gas kinematics regardless the absolute values for each quantities in each model.

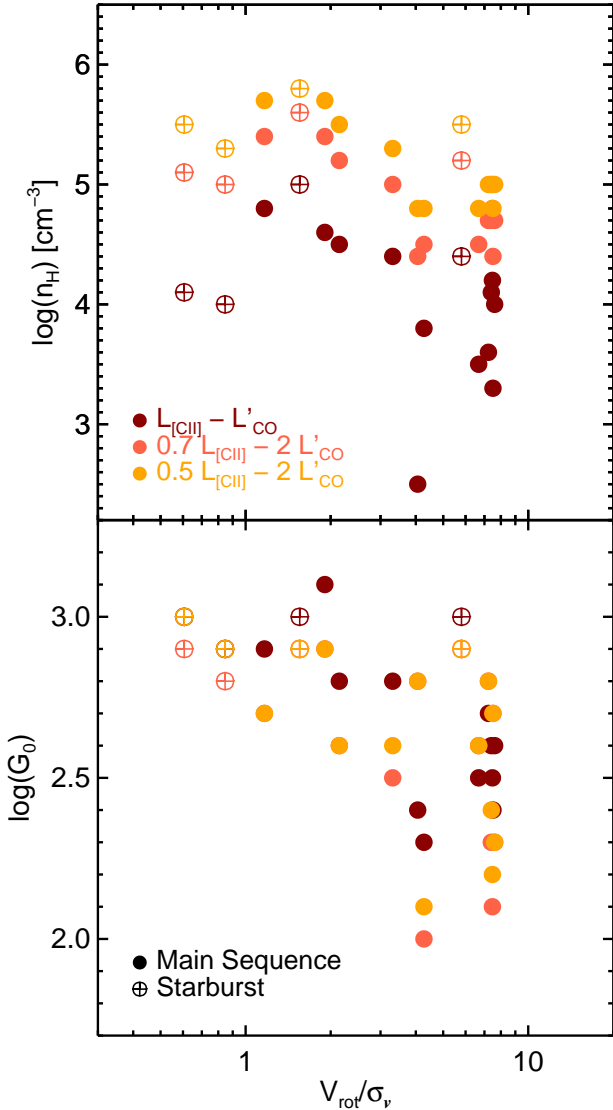


**Figure 8.** Hydrogen nuclei density ( $n_H$ , *top*) and incident FUV radiation strength ( $G_0$ , *bottom*) as a function of  $V_{\text{rot}}/\sigma_v$  ratio for our sample. We colour-code the data depending on the [C II] and CO(1-0) luminosities used to constrain the physical parameters through the PDR modelling (see § 4.3 for more details). We also classify the sources as ‘starburst’ or ‘normal’ star-forming galaxy. Regardless of the PDR model, galaxies with low  $V_{\text{rot}}/\sigma_v$  ratio tend to show higher hydrogen nuclei density and  $G_0$  values. We note that  $G_0$  seems to be insensitive to the [C II] and CO(1-0) luminosities assumed to constrain the PDR model within our sample.

In Fig. 8 we compare  $n_H$  and  $G_0$  as a function of the  $V_{\text{rot}}/\sigma_v$  ratio for each model within our sample. We do not consider the galaxies with  $n_H \lesssim 10^2 \text{ cm}^{-3}$  due to the high degeneracy of the model in the parameter space (Hughes et al. 2017a). In the top panel we see how the hydrogen nuclei density may increase at low  $V_{\text{rot}}/\sigma_v$  for each PDR modelling. This is consistent with the picture in which higher density environments usually show higher velocity dispersions. In the bottom panel, the incident FUV radiation strength also increases at low  $V_{\text{rot}}/\sigma_v$  for each PDR modelling.  $G_0$  seems to be nearly independent of the assumed [C II] and CO(1-

0) luminosities to constrain the PDR model, the variation of  $G_0$  across our sample may reflect the variation of SFR through the IR-luminosity. Therefore, the trend between  $G_0$  and  $V_{\text{rot}}/\sigma_v$  seen in Fig. 8 may reflect the  $L_{\text{IR}} - V_{\text{rot}}/\sigma_v$  correlation observed in § 4.2.3.

If systems with high  $G_0$  – i.e. high SFR (or  $L_{\text{IR}}$ ) and low  $V_{\text{rot}}/\sigma_v$  – have ionized most of their atomic carbon content within the PDRs, then this should result in an inefficient gas cooling through the [C II] emission line and a lack of the observed [C II] luminosity compared to the IR luminosity. This may explain the ‘[C II] deficit’ correlation with galactic dynamics found in § 4.2.3.

#### 4.4 Dynamical Masses of Turbulent Thick Galactic Disks

The dynamical mass estimate ( $M_{\text{dyn}}$ ) is a major tool that allows to measure the mass of galaxies, and a simple way to probe the existence of dark matter haloes (e.g. Gnerucci et al. 2011). By considering galaxies as thin disks, in which all the material is supported by rotation [ $M_{\text{dyn,thin}}(r) = \frac{V_{\text{rot}}^2(r)r}{G}$ ], the dynamical mass can be easily derived from the two-dimensional kinematic modelling (e.g. Genzel et al. 2011). However, galaxies with low  $V_{\text{rot}}/\sigma_v$  ratio are believed to be well-represented by galactic thick disks (e.g. Glazebrook 2013). In those galaxies, a considerable pressure support is needed to be taken into account in order to calculate reliable dynamical mass estimates (Burkert et al. 2010).

In order to test whether the galaxies in our sample are better represented by galactic thick disks rather than thin disks we calculate their dynamical masses and compare with their stellar masses (Table 2). Following Burkert et al. (2010), we model our galaxies as turbulent galactic gas disks in which pressure support cannot be neglected. In this model, the *observable* rotational velocity is given by:

$$V_{\text{rot}}^2 = V_0^2 + 2\sigma_v^2 \frac{d \ln \Sigma}{d \ln r}, \quad (2)$$

where  $V_0$  is the zero-pressure velocity curve ( $V_0^2 \equiv r \times d\Phi/dr$ ), which traces the gravitational potential of the galaxy;  $\sigma_v$  is the one-dimensional velocity dispersion of the gas, and  $\Sigma$  is the total mass surface density profile of the galaxy. In order to derive an explicit model from of Eq. 2 we need to make some assumptions about the total mass surface density distribution  $\Sigma(r)$ . Assuming both, that  $\Sigma$  follows the stellar mass surface density profile ( $\Sigma_*$ ) and constant  $K$ -band mass-to-light ratio across the galactic disk ( $\Upsilon_K$ ), then  $\Sigma$  can be approximated by the  $K$ -band surface brightness distribution ( $\mu_K$ ), i.e.  $\Sigma(r) \approx \Sigma_*(r) \approx \Upsilon_K \mu_K(r)$ . Considering that  $\mu_K$  is well-described by a Sérsic profile (Sérsic 1963), Eq. 2 can be written as:

$$V_{\text{rot}}^2 = V_0^2 - \frac{2\sigma_v^2 b_{n_S}}{n_S} \left(\frac{r}{r_e}\right)^{1/n_S}, \quad (3)$$

where  $n_S$  is the Sérsic index and  $b_{n_S}$  is the Sérsic coefficient, which sets  $r_e$  as the half-light radius. We note that the case  $n_S = 1$  is equivalent to an exponential profile. In this model, the dynamical mass is traced by  $V_0^2$  rather than  $V_{\text{rot}}^2$ :

$$M_{\text{dyn,thick}}(r) = \frac{V_0^2(r)r}{G}. \quad (4)$$

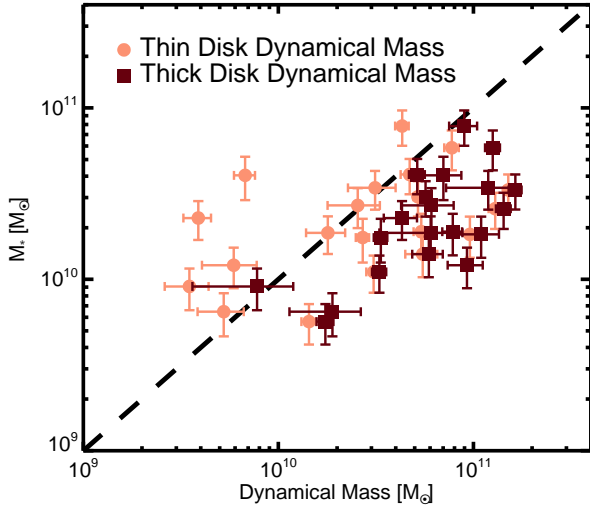


**Figure 9.** Encircled stellar masses at the radii at which  $V_{\text{rot}}$  is extracted ( $2 r_{1/2, \text{CO}}$ ) as a function of the dynamical masses encircled at the same radius. The light-red circles show the dynamical masses assuming a thin disk model, i.e. the total mass is traced just by the observed rotational velocity. The dark red squares show the dynamical masses assuming a thick disk model in which the surface density profile of each galaxy is traced by the  $K$ -band surface brightness also assuming a constant mass-to-light ratio. The encircled stellar mass content is calculated by considering the  $\mu_K$  profile (see Eq. 5). The dashed line corresponds to the 1:1 ratio. We clearly see how the thin disk approximation fails to estimate the total mass in five systems as their truncated stellar masses have greater values.

We note that the  $K$ -band Sérsic model parameters for our resolved sample are listed in Table 1 for each galaxy. For the galaxy without  $K$ -band modelling, we assume an exponential  $\Sigma_*$  profile.

In Fig. 9 we show the dynamical masses calculated by assuming a thin disk model and a thick disk model (Eq. 4) within  $r \leq 2r_{1/2, \text{CO}}$ . We note that we have considered the radius at which we extracted  $V_{\text{rot}}$ . We compare these dynamical masses with the stellar masses truncated at the same radius and normalized to the stellar mass values derived in V17 (Table 2):

$$M_*(r) \equiv M_* \frac{\int_{S(<r)} \Sigma_*(r) dS}{\int_S \Sigma_*(r) dS} \approx M_* \frac{\int_0^r \mu_K(r) r dr}{\int_0^\infty \mu_K(r) r dr}. \quad (5)$$

The dashed line in Fig. 9 represents the 1:1 ratio between both quantities. Clearly, the thin disk dynamical mass model underestimates the total mass for five of our systems, as it predicts masses lower than the stellar masses. On the other hand, the thick disk dynamical mass model estimates masses greater than the stellar masses, with just one target showing stellar mass nearly equal to their estimated dynamical mass within  $1 \sigma$  error. This suggests that these five VALES galaxies with lower  $V_{\text{rot}}/\sigma_v$  ratio may be better represented by thick galactic disk, while the rest of the sample is best described by thin galactic disk. We note that the existence of gaseous thick disks at the observed redshift range may indicate a late assembly of the thick disk stellar com-

ponent in those systems (Bournaud, Elmegreen & Martig 2009).

The validity of this result depends on the assumption that the  $K$ -band surface brightness traces  $\Sigma_*$  by considering a mass-to-light ratio which does not vary as a function of galactocentric radius. We explore the effect produced by a different mass distribution in Appendix A, where we show that it has a negligible effect when considering, for example, an exponential disk mass profile. We conclude that the considerable pressure support predicted by the high velocity dispersion values is a key ingredient to obtain reliable conclusions from the modelling. This may be especially important in the systems which present the highest gas fractions (see § 4.6).

We caution, however, that spatial resolutions effects may produce an overestimation or underestimation of the dynamical mass values derived from the thin and thick disk models. The  $V_{\text{rot}}$  values can be underestimated by beam smearing, especially in cases when the rotation curve beyond the turn-over radius is not observed (e.g. HATLASJ084217.7+021222). On the other hand, overestimated  $r_{1/2, \text{CO}}$  and  $\sigma_v$  values are expected to be calculated due to the same effect. The result of the competition between both effects is uncertain. Thus, high spatial resolution observations are required to obtain more accurate dynamical mass estimates.

#### 4.5 Gravitationally stable disks

Gravitational stability analysis is usually used to explain the formation and growth of internal galactic sub-structures at low (e.g. Lowe et al. 1994) and high redshifts (Swinbank et al. 2012b; Wisnioski 2012), between other major topics (e.g. Kennicutt 1998b). In thin galactic disks, gravitational stability was first studied by Toomre (1964), who derived a simple criterion that can be quantified through the stability parameter:

$$Q_{\text{Toomre}} \equiv \frac{\kappa \sigma_v}{\pi G \Sigma_{\text{gas}}}, \quad (6)$$

where,  $\kappa \equiv (2\Omega/r) d(r^2\Omega)/dr = av_c/r$  is the epicyclic frequency, usually expressed as a function of orbital frequency ( $\Omega$ ) or the circular velocity  $v_c$  at some radius  $r$  with  $a = \sqrt{2}$  for a flat rotational curve;  $\sigma_v$  is the measure of the random motions of the gas;  $\Sigma_{\text{gas}}$  is the gas surface density; and  $G$  is the gravitational constant. If  $Q_{\text{Toomre}} < 1$ , then the system is prone to develop local gravitational instabilities. Otherwise ( $Q_{\text{Toomre}} > 1$ ), the system is not susceptible to local gravitational collapse.

Since the Toomre (1964)'s earlier work, the  $Q_{\text{Toomre}}$  parameter has been generalized to include different physical effects such as galactic disk thickness ( $Q_{\text{thick}}$ , e.g. Goldreich & Lynden-Bell 1965; Romeo 1992) and/or multiple galactic components ( $Q_M$ , e.g. Jog & Solomon 1984; Jog 1996; Rafikov 2001; Romeo & Wiegert 2011):

$$Q_{\text{thick}} = T Q_{\text{Toomre}}, \quad (7)$$

$$\frac{1}{Q_M} = \sum_{k=1}^M \frac{W_k}{Q_{\text{Toomre}, k}}, \quad (8)$$

where,  $T$  represents the stabilizing effect of the disk thickness, and ranges between 1–1.5 depending on the velocity dispersion anisotropy ( $\sigma_{v,z}/\sigma_{v,R}$ ; Romeo & Wiegert 2011).  $Q_{\text{Toomre},k}$  is the Toomre parameter of component  $k$ ,  $M$  is the total number of different galactic components considered in the analysis, and  $W_k$  is a weighting factor that is higher for the component with smallest  $Q_{\text{Toomre}}$  value (see Romeo & Falstad 2013 for more details). Other physical effects such as gas dissipation (e.g. Elmegreen 2011), and supersonically turbulence (e.g. Romeo, Burkert & Agertz 2010) can be included to derive other generalized  $Q$  parameters, however they required assumptions on how the gas dissipates energy across different scales and its beyond the scope of this work test those assumptions. Thus, in order to maintain simplicity, we just test the  $Q_{\text{Toomre}}$ ,  $Q_{\text{thick}}$  and the  $Q_M$  stability parameters and for the  $Q_M$  parameter we just consider the stellar and molecular gas galactic components ( $M = 2$ ).

In order to proceed further, by assuming that; (1) the system is supported by rotation; (2) the galactic mass budget is dominated by the gas and stars at the radii in which  $V_{\text{rot}}$  is derived; and (3) the gas within that radii is principally in the form of molecular gas; then the  $Q_{\text{Toomre}}$  (hereafter,  $Q_{\text{gas}}$ ) can be rewritten as a function of the molecular gas kinematics and the molecular gas fraction (Genzel et al. 2011):

$$Q_{\text{gas}} \approx \sqrt{2} \frac{\sigma_v}{v_c} f_{\text{H}_2}^{-1}. \quad (9)$$

By following an analogous procedure, we find similar formulas for the  $Q_{\text{thick}}$  and  $Q_M$  (hereafter,  $Q_2$ ) parameters:

$$Q_{\text{thick}} \approx T \sqrt{2} \frac{\sigma_v}{v_c} f_{\text{H}_2}^{-1}, \quad (10)$$

$$Q_2 \approx \begin{cases} \sqrt{2} \frac{\sigma_v}{v_c} [f_{\text{H}_2} + \frac{2}{1+s^2}(1-f_{\text{H}_2})]^{-1} & \text{if } s > \frac{1}{f_{\text{H}_2}} - 1; \\ \sqrt{2} \frac{\sigma_v}{v_c} [\frac{2s}{1+s^2} f_{\text{H}_2} + \frac{1}{s}(1-f_{\text{H}_2})]^{-1} & \text{otherwise,} \end{cases} \quad (11)$$

where ‘ $s$ ’ is the stellar to molecular gas velocity dispersion ratio ( $s \equiv \sigma_*/\sigma_v \geq 1$ ) and the conditioning represents the  $Q_{\text{stars}} > Q_{\text{gas}}$  requirement (see Romeo & Falstad 2013, for more details).

In order to fulfil assumption (1), we choose  $M_{\text{dyn,thin}}/M_{\text{dyn,thick}} > 0.5$  as a somewhat crude criterion to select galaxies that are mainly supported by rotation. Regardless of the density profile of the galaxies, this criterion can be traduced into a threshold to the measured  $V_{\text{rot}}/\sigma_v$  ratio ( $V_{\text{rot}}/\sigma_v \gtrsim 2$  in our case). Thus, within our resolved sample, we just find 11 galaxies consistent with being rotationally supported.

In Fig. 10 we show  $f_{\text{H}_2}$  as a function of  $V_{\text{rot}}/\sigma_v$  for the rotationally supported galaxies in our sample. The orange dot-dashed, dashed and dotted lines represent the  $Q_{\text{gas}} = 2, 1, 0.5$  values, respectively. Three galaxies are consistent with  $Q_{\text{gas}} \sim 1$  (within  $1\sigma$  range), whilst eight galaxies have  $Q_{\text{gas}} \gtrsim 2$ . The majority of our rotationally supported systems seems to be gravitationally unstable within the thin disk single component approximation. Although the poor spatial resolution of our observations smooth the CO intensity maps, we note that the unique source that shows some degree of clumpiness in its CO intensity map (HATLASJ085340.7+013348) is consistent with being susceptible to gravitational instabilities.

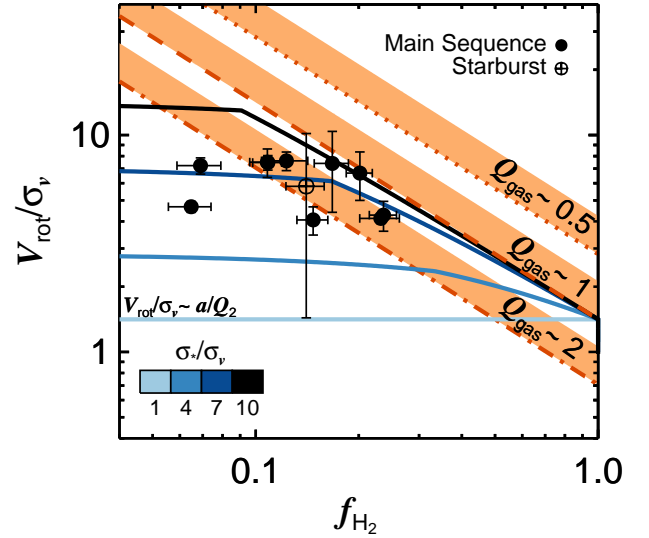


**Figure 10.**  $V_{\text{rot}}/\sigma_v$  as a function of the molecular gas fraction. The orange dotted-dashed, dashed and dotted lines represent the Toomre (1964)’s  $Q_{\text{gas}}$  values of 2, 1 and 0.5 for thin disk galaxies, respectively. The orange-shaded areas represent the possible  $Q_{\text{thick}}$  values given the mentioned  $Q_{\text{gas}}$  values. The black, dark-blue, blue and light-blue lines shows the  $Q_2 = 1$  values for different  $\sigma_*/\sigma_v$  ratios listed in the colorbar. We also classify the sources as ‘starburst’ or ‘normal’ star-forming galaxy.

The next step is to include the disk thickness effect in our analysis. In order to do that, we use Eq. 7 to compute  $Q_{\text{thick}}$  from the  $Q_{\text{gas}} = 2, 1, 0.5$  values. As we do not have velocity dispersion anisotropy estimates for our sample to determine the  $T$  factor, we assume  $T$  values between the limit ranges ( $1 \leq T \leq 1.5$ ; Romeo & Wiegert 2011) and we present the possible  $Q_{\text{thick}}$  values as the orange-shaded areas in Fig. 10. From our sample, is clearly that we can not differentiate the disk thickness effect through the gravitational stability analysis as our kinematic estimates are not enough accurate.

As a final step, we consider a two-component gravitational stability analysis in which the main components are the molecular gas and the stars. We note that the two-component system is more unstable than either component in the system by itself (Jog 1996). However, in order to use the two-component gravitational stability criterion ( $Q_2$ ), we must measure  $\sigma_*$ , the velocity dispersion of the stars, or in equivalence the  $\sigma_*/\sigma_v$  ratio. As we lack of that information for our rotationally supported galaxies, we just assume four different values of  $\sigma_*/\sigma_v$ , between the range indicated in the colorbar in Fig. 10. We note that  $\sigma_*/\sigma_v = 1$  is the minimum value that can be assumed within this model (see Romeo & Falstad 2013 for more details). On the other hand, a maximum range value of  $\sigma_*/\sigma_v = 10$  may be appropriate for local spiral galaxies. For example, the expected value for the Milky Way is in the range of  $4 < \sigma_*^{\text{MW}}/\sigma_v^{\text{MW}} < 8$ , whether we consider the stellar velocity dispersion of the thin or thick disk as the representative  $\sigma_*^{\text{MW}}$  value (Glazebrook 2013). In the remaining of our analysis we kept fixed  $Q_2$  to the unity value.

At high  $\sigma_*/\sigma_v$  ratio, the molecular gas component is

more susceptible to gravitational instabilities than stars, and therefore, the gravitational stability of the system is dictated by the gaseous component alone ( $Q_2 \approx Q_{\text{gas}}$ ) at least if  $f_{\text{H}_2}$  is not low enough. The latter case implies  $Q_2 \approx Q_{\text{stars}}$ . In Fig. 10, the  $Q_2 \approx Q_{\text{gas}}$  case is better represented by the black line, which approach to the orange-dashed line ( $Q_{\text{gas}} = 1$ ) at  $f_{\text{H}_2} \gtrsim 0.1$ . For molecular gas fractions below that value, the gravitational stability of the system is dictated mainly by the stellar component from which we do not have any information. We also note that when the  $\sigma_*/\sigma_v$  ratio decreases,  $Q_2$  approximates to  $Q_{\text{gas}}$  at higher  $f_{\text{H}_2}$  values as the gravitational effect of the stellar component becomes more significant.

At  $\sigma_*/\sigma_v \sim 1$ , from Eq. 11 we can see that the  $Q_2$  parameter does not depends on  $f_{\text{H}_2}$ . In this limit, the two-component system behave as a single component fluid in which the gravitational criterion is dictated by the total surface density of the system. In Fig. 10 it is better represented by the light-blue line. In this limit, the  $Q_2$  value can be recovered by measuring the kinematics of the galaxy and the shape of the rotation curve (accounted by the factor  $a$ ) at a given radii. Nevertheless, if the dark matter component is not negligible, i.e. assumption (2) is incorrect, then an additional baryonic mass fraction needs to be accounted.

Within two-fluid component framework, two of the rotationally supported galaxies are consistent with being gravitational unstable systems (within  $1\sigma$  range). The seven galaxies with the lower  $f_{\text{H}_2}$  values are likely to be in the  $Q_2 \approx Q_{\text{stars}}$  regime. Thus, we can not determine if these systems are gravitationally stable or not. We also note that the remaining galaxies can be consistent with being gravitationally unstable or not depending on its  $\sigma_*$  value.

Therefore, from the gravitational stability analysis we conclude that two galaxies are consistent with being marginally gravitationally unstable disk, but observations of the stellar dynamics are required to determine the gravitational stability for the remaining nine cases.

This result disagrees with White et al. (2017) who found a  $Q_{\text{gas}} \sim 1$  trend in their sample of local star-forming galaxies taken from the DYNAMO survey ( $z \sim 0.06 - 0.08$  &  $z \sim 0.12 - 0.16$ ). They found this trend by fitting the Eq. 9 (their Eq. 10) to their sample, but by considering ionized gas kinematics instead molecular gas kinematics.

We note that our conservative choice of  $\alpha_{\text{CO}}$  values (see § 2.2) tends to overestimate the molecular gas reservoir for most of the galaxies within our sample. Using a lower CO-to-H<sub>2</sub> conversion factor would imply greater  $Q_{\text{gas}}$ ,  $Q_{\text{thick}}$  and  $Q_2$  values in these galaxies.

Nevertheless, we have analysed the galaxies in which the assumption (1) is likely to be correct, however we can not determine if assumptions (2) and (3) are correct. We stress that HI observations are required in order to test assumptions (2) and (3).

#### 4.6 Energy sources of turbulent motions

The origin of the energy sources of the random motions in galactic disks are unclear, low and high- $z$  galaxy observations show a positive correlation between the ionized gas turbulence with the measured  $\Sigma_{\text{SFR}}$ , with larger scatter at high- $z$  (e.g. Lehnert et al. 2009; Johnson et al. 2018; Zhou et al. 2017). These observations favour a models in which

stellar feedback is driving those random motions. However, observations also suggest that other energy sources may contribute to produce turbulence in the ISM (Zhou et al. 2017).

From a theoretical perspective, two possible scenarios have been proposed. In the first scenario, the star-formation is determined by the requirement to maintain hydrostatic balance through the input of energy from supernovae feedback. In this model, stars are produced efficiently by the gravitational collapse of gas within GMCs and the GMCs are treated as bound entities that are hydrodynamically decoupled from the galactic disk (Faucher-Giguère, Quataert & Hopkins 2013). Therefore, the production of stars is limited by the formation of GMCs and this process is driven by the self-gravity of the gas, and not by a combination of the gravitational potential of gas and stars from the galactic disk. Thus, in the feedback-driven model, it is expected that  $\text{SFR} \propto \sigma_v^2$ . In the second scenario, the turbulence is expected to be driven by the release of gravitational energy of the gas which is accreted through the disk (Krumholz & Burkhardt 2016). The accretion of the gas is ultimately powered by gravitational instabilities through the galactic disk that are regulated by the gravitational potential of stars and gas. This model also assumes a star formation law in which the star formation rate per molecular gas mass is represented by  $\epsilon_{\text{ff}}/t_{\text{ff}}$ , the efficiency per free-fall time ( $\epsilon_{\text{ff}} \approx 0.01$ , e.g. Krumholz & Tan 2007; Krumholz, Dekel & McKee 2012). The  $t_{\text{ff}}$  is estimated by assuming that the star-forming gas density is set by the total gravitational potential of the ISM, rather than by the properties of hydrodynamically decoupled GMCs (Krumholz, Dekel & McKee 2012). In this gravity-driven model, the SFR vary as  $\text{SFR} \propto \sigma_v f_{\text{gas}}^2$ , where  $f_{\text{gas}}$  is the mid-plane galactic gas fraction.

With the aim to test both models, in the top and bottom panels of Fig 11 we show  $f_{\text{H}_2}$  and  $\sigma_v$  as a function of the SFR, for the VALES survey and the Extragalactic Database for Galaxy Evolution Survey selected from the Calar Alto Legacy Integral Field Area sample (EDGE-CALIFA) (Bolatto et al. 2017). The VALES data are colour-coded in each panel by the velocity dispersion and the molecular gas fraction, respectively. The EDGE-CALIFA data are represented by the dark-grey triangles. The EDGE-CALIFA data were modelled using the same procedure described for the VALES data (see § B for more details). In top panel, we also show the median  $f_{\text{H}_2}$  and SFR values per  $\log_{10}(f_{\text{H}_2}) = 0.4$  bin combining the data from both surveys. The median values suggest that the SFR is weakly correlated with  $f_{\text{H}_2}$ . Systems with high molecular gas fraction may tend to have high SFR, although the scatter is considerable. On the other hand, in the bottom panel, we observe that systems with high SFRs also tend to present high  $\sigma_v$  values. We note that we do not find any correlation between inclination angles and velocity dispersions within Fig 11.

We represent the best-fitted gravity-driven and feedback-driven models by the dashed and dotted lines in Fig. 11, respectively. The gravity-driven model gives a poor description to the data. At high molecular gas fractions ( $f_{\text{H}_2} \gtrsim 0.1$ ), galaxies tend to present a large variety of SFRs than the predicted by this model. This suggests that the release of the gravitational energy from the molecular gas may not be the main source of energy that support the  $\sigma_v$  values observed in the VALES and EDGE-CALIFA surveys. The feedback-driven model may also not explain the



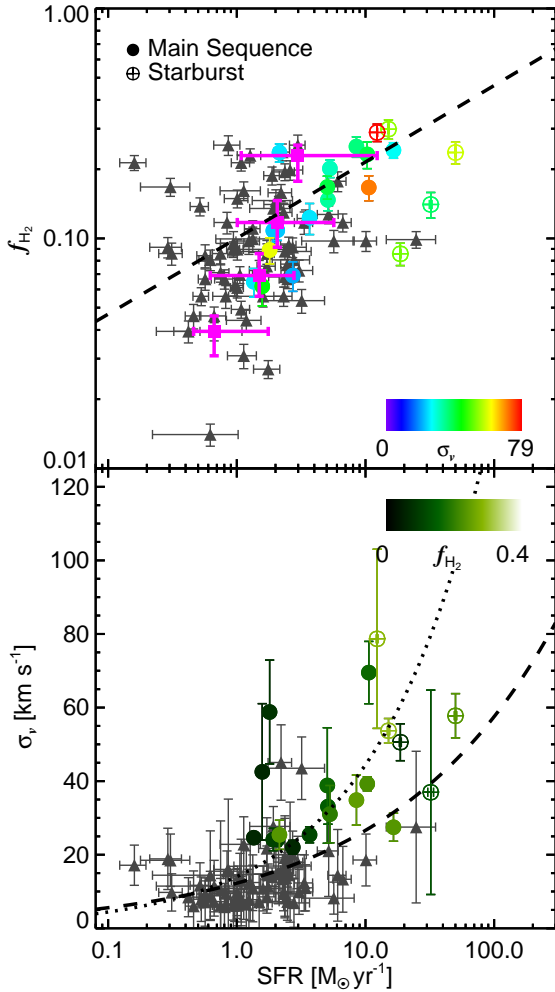


**Figure 11.** *Top:* Molecular gas fraction as a function of SFR, colour-coded by velocity dispersion. *Bottom:* Velocity dispersion as a function of SFR. We colour-coded the VALES galaxies by molecular gas fraction. In both panels the VALES galaxies are classified as ‘normal’ (filled circles) and ‘starburst’ (circles with plus sign) star-forming galaxies. The dark grey triangles represent the galaxies from the EDGE-CALIFA survey (Bolatto et al. 2017). In the top panel, the magenta squares represent the median  $f_{\text{H}_2}$  and SFR values per  $\log_{10}(f_{\text{H}_2}) = 0.4$  bin. The dashed line represents the best-fitted gravity-driven model ( $\text{SFR} \propto \sigma_v f_{\text{gas}}^2$ ) for the VALES galaxies; Krumholz & Burkhardt (2016), assuming  $f_{\text{gas}} \approx f_{\text{H}_2}$ . The dotted line in the bottom panel represents the best-fitted feedback-driven model for the VALES galaxies ( $\text{SFR} \propto \sigma_v^2$ ; Faucher-Giguère, Quataert & Hopkins 2013).

loci of the galaxies in the  $\text{SFR}-f_{\text{H}_2}-\sigma_v$  phase space as it tends to overestimate the  $\sigma_v$  values for most of the systems with  $\text{SFR} \gtrsim 2 M_{\odot} \text{yr}^{-1}$ . The distribution of the VALES and EDGE-CALIFA galaxies in Fig. 11 suggest that different energy sources may sustain the observed supersonic turbulence.

We stress that the scatter behind Fig. 11 might be induced by a handful of effects, including the bimodal CO-to- $\text{H}_2$  conversion factor (see § 2.1) used to calculate the molecular gas masses and, therefore, the molecular gas fractions. On the other hand, poor spatial resolution could potentially bias  $\sigma_v$  towards higher values. It may contribute to the high

velocity dispersion values seen in the VALES galaxies with higher SFRs. Spatial resolution effects may favour models which accounts for a higher dependence of the SFR with  $\sigma_v$ .

Despite of the weakness of the median trend observed between SFR and  $f_{\text{H}_2}$ , we note that this result is in contradiction with Green et al. (2010) results. They found that velocity dispersion values measured from a sample of 65 star-forming galaxies at  $z \sim 0.1$  seems to be correlated with their SFRs but not with the gas fraction. However, as a difference with our work, they estimated the velocity dispersion values from the ionized gas kinematics traced by the  $\text{H}\alpha$  emission line, whilst we are observing the molecular gas kinematics. Moreover, Green et al. (2010) calculated the gas mass content for their sample by converting the measured  $\Sigma_{\text{SFR}}$  through the application of the KS law, this assumes that the molecular and ionized gas are spatially correlated, but also that the galaxies in their sample follow the KS law, which is not straightforward to assume (see § 4.7). On the other hand, we measure the molecular gas content from the CO line emission by applying the CO-to- $\text{H}_2$  conversion factor. Nevertheless, we stress that spatially resolved observations of gas-rich systems ( $f_{\text{H}_2} \gtrsim 0.3$ ) are needed to refute or probe possible trends between SFR and  $f_{\text{H}_2}$ .

It should be mentioned that the model developed by Krumholz & Burkhardt (2016) relates the SFR with the mid-plane galactic gas fraction and its velocity dispersion rather than the molecular gas fraction and the molecular gas velocity dispersion which are shown in Fig 11. We note that it is not straightforward to expect that those quantities are related between each other. The model also assumes that the stellar velocity dispersion should be comparable with the velocity dispersion of the gas. Taking into account these caveats, in order to produce a more complete observational test, atomic gas (HI) and stellar kinematic observations are needed.

#### 4.7 Kennicutt-Schmidt Law Efficiency & Depletion Times

The Kennicutt-Schmidt law (Kennicutt 1998a,b) describes the power-law relationship between the galaxy star formation rate surface density and the disk-averaged total gas surface density. It describes how efficiently galaxies turn their gas into stars. For local galaxies, this correlation is well-fitted by  $\Sigma_{\text{SFR}} \propto \Sigma_{\text{gas}}^{1.4}$ . (Kennicutt 1998b). Although a tight relation can be found when  $\Sigma_{\text{SFR}}$  is compared with the molecular gas surface density  $\Sigma_{\text{H}_2}$  rather than  $\Sigma_{\text{gas}}$  (e.g. Bigiel et al. 2008; Leroy et al. 2008, 2013), also the slope is changed ( $\Sigma_{\text{SFR}} \propto \Sigma_{\text{H}_2}$ ).

However, the KS law shows an apparent bimodal behaviour where ‘disks’ and ‘starburst’ galaxies fill the  $\Sigma_{\text{H}_2}-\Sigma_{\text{SFR}}$  plane in two parallel sequences (Daddi et al. 2010). Nevertheless, by computing  $\Sigma_{\text{H}_2}/t_{\text{ff}}$  and/or  $\Sigma_{\text{H}_2}/t_{\text{orb}}$  relationships, a single power-law relation can be obtained (e.g. Daddi et al. 2010; Krumholz, Dekel & McKee 2012). The  $\Sigma_{\text{SFR}}-\Sigma_{\text{H}_2}/t_{\text{ff}}$  relation can be interpreted as dependence of the star formation law on the local volume density of the gas, whilst the  $\Sigma_{\text{SFR}}-\Sigma_{\text{H}_2}/t_{\text{orb}}$  relation suggests that the star formation law is affected by the global rotation of the galaxy. Thus, the relevant timescale gives us critical information about the physical processes that may control the formation of stars.

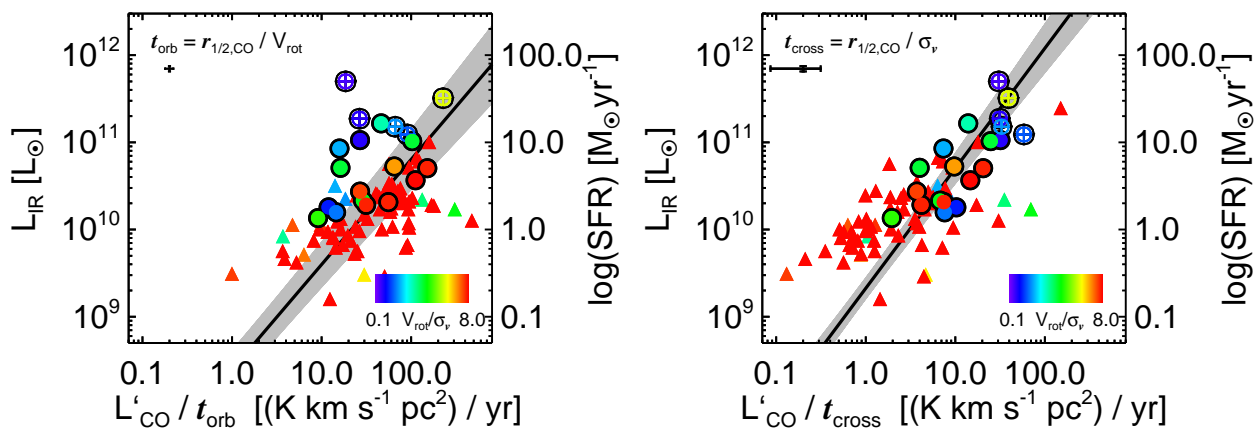


**Figure 12.** The IR luminosity as a function of the CO luminosity divided by the orbital timescale (left panel) and the crossing time (right panel). In both panels the VALES galaxies are classified as ‘normal’ (filled circles) and ‘starburst’ (circles with plus sign) galaxies as in Fig. 6. The triangles represent the EDGE-CALIFA galaxies (Bolatto et al. 2017). The VALES and CARMA-EDGE data presented in both panels are colour-coded by the observed  $V_{\text{rot}}/\sigma_v$  ratio. The line and the grey shaded area represent the best-fitted power-law function and its  $1\sigma$  error respectively in each panel. For the  $\text{SFR}-L'_{\text{CO}}/\tau_{\text{orb}}$  plot (left panel) we find a best-fit slope of  $1.21\pm 0.14$ , whilst for the  $\text{SFR}-L'_{\text{CO}}/\tau_{\text{cross}}$  plot (right panel) we find a best-fit slope of  $1.38\pm 0.13$ .

Although we are considering just galaxies where their CO luminosity is spatially resolved (see 2.1), we do not have any information of the spatial extent of the IR luminosity, i.e. the SFR. Therefore, to study the KS law and its dependence on different timescales we need to assume the spatial extent of the SFR within each galaxy. However, in order to avoid the need of this assumption, instead of using the surface density quantities  $\Sigma_{\text{H}_2}$  and  $\Sigma_{\text{SFR}}$ , we use the spatially integrated variables. We also try not to assume a specific CO-to- $\text{H}_2$  conversion factor, thus, we finally use the SFR (from  $L_{\text{IR}}$ ) and  $L'_{\text{CO}}$  galactic quantities (Table 2).

In Fig. 12 we investigate whether the star formation activity occurs on a timescale set by the orbital time ( $t_{\text{orb}} \equiv r_{1/2,\text{CO}}/V_{\text{rot}}$ ; left panel) or the crossing time ( $t_{\text{cross}} \equiv r_{1/2,\text{CO}}/\sigma_v$ ; right panel) by studying the  $\text{SFR}-L'_{\text{CO}}/t_{\text{orb}}$  and  $\text{SFR}-L'_{\text{CO}}/t_{\text{cross}}$  correlations, respectively. We just consider these two timescales as they can be calculated directly from our molecular gas ALMA observations. We also include the data presented in the EDGE-CALIFA survey (Bolatto et al. 2017). These data were modelled using the same procedure described for the VALES data (see § B for more details).

In the left panel of Fig. 12 we find that galaxies with high SFRs also tend to present high  $L'_{\text{CO}}/t_{\text{orb}}$  ratios. The Spearman’s rank correlation coefficient is 0.52 with a significance of its deviation from zero of  $1.3\times 10^{-7}$ . Thus, we find a correlation between SFR and  $L'_{\text{CO}}/t_{\text{orb}}$  in our data. The data are fitted by a power-law function with best-fit slope of  $1.21\pm 0.14$ . However, we note that the VALES galaxies with low  $V_{\text{rot}}/\sigma_v$  ratio tend to lie above this fit, suggesting an enhanced star-formation efficiency per orbital time in these systems, in contradiction with Daddi et al. (2010). Although this correlation is often used to suggest that global galactic rotation may affect the star formation process (e.g. Silk 1997), we note that, perhaps, this explanation may not be the unique.

Galaxies with higher SFRs are expected to be more massive and have large gas content. Also, a massive galaxy is expected to rotate faster in order to balance its self-gravity. Therefore, the  $\text{SFR}-L'_{\text{CO}}/t_{\text{orb}}$  correlation may reflect

the mass-velocity trend in galaxies. We note that the location of the galaxies with low  $V_{\text{rot}}/\sigma_v$  ratio in the  $\text{SFR}-L'_{\text{CO}}/t_{\text{orb}}$  plane can also be explained by the same kind of argument, but by considering a more sophisticated hydrodynamical balance against the gravitational force. In § 4.4 we found that five systems are better represented by thick galactic disks than thin galactic disks. In thick disks, the gravitational force is balanced by both, negative radial pressure gradients and rotational support. Thus, thick galactic disks present lower  $V_{\text{rot}}$  values compared to thin galactic disks with equivalent mass. Therefore, the apparently enhanced star formation efficiency per orbital time observed in the  $\text{SFR}-L'_{\text{CO}}/t_{\text{orb}}$  plane for galaxies with low  $V_{\text{rot}}/\sigma_v$  ratio in our sample may be produced by a relative reduction of the rotational velocity as pressure support is not negligible across their galactic disk.

Within the thick disk model (Burkert et al. 2010), the relevance of the pressure support is reflected by the velocity dispersion value (Eq. 2). Thus, one possible way to test the pressure support influence on the star formation is to test dependence of the SFR on the timescale given by  $\sigma_v$ , the crossing time. We remind that the velocity dispersion range observed in our sample is  $\sigma_v \sim 22 - 79 \text{ km s}^{-1}$  (Table 2). In the right panel of Fig. 12 we plot the SFR as a function of  $L'_{\text{CO}}/t_{\text{cross}}$ . We also find that galaxies with high SFR tend to have greater  $L'_{\text{CO}}/t_{\text{orb}}$  ratio. The Spearman’s rank correlation coefficient is 0.69 with a significance of  $5.6\times 10^{-13}$ , also suggesting a correlation between both quantities. The best-fit power law function is  $1.38\pm 0.13$ . The  $\text{SFR}-L'_{\text{CO}}/t_{\text{cross}}$  represents a reasonably better fit to data. However, we caution that the fitting procedures are highly sensitive on whether we include the starburst galaxies or not in our data, i.e., the parameter errors may be underestimated.

Another way to study the star-formation law is by defining the ‘star formation efficiency’ parameter as the star formation rate divided by the CO(1-0) luminosity ( $\text{SFE}' \equiv \text{SFR}/L_{\text{CO}}$ ), i.e. a proxy of the molecular depletion time without assuming any  $\alpha_{\text{CO}}$  factor can be obtained by calculating  $L'_{\text{CO}}/\text{SFR}$  (Cheng et al. 2018). This depletion

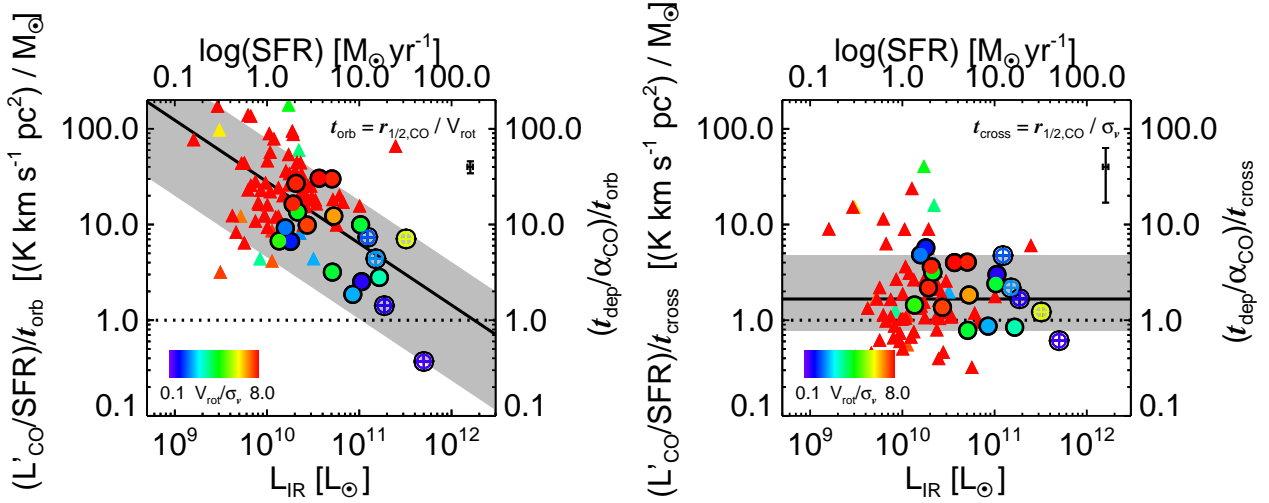


**Figure 13.** The  $L'_{\text{CO}}/L'_{\text{IR}}$  ratio ( $\text{SFE}'^{-1}$ ) divided by the orbital time (left) and crossing time (right) as a function of the IR-luminosity (SFR). This can be interpreted as the molecular gas depletion time divided by the respective timescale (orbital or crossing time) as a function of the SFR, without any assumption of the CO-to- $\text{H}_2$  conversion value. The data presented in both panels are coded in the same way as Fig. 12). The dotted lines represent a 1:1 ratio. In the left panel, the black line shows the best-fitted power-law function and the  $1\sigma$  error is represented by the grey-shaded region. In the right panel, the black line shows the median value and the grey shaded region also represents the  $1\sigma$  region. Interestingly, the data is consistent with a star formation law in which our proxy of depletion time is fixed per crossing time.

time proxy can be compared with other timescales ‘ $t$ ’ by calculating the  $(L'_{\text{CO}}/\text{SFR})/t$  ratio. If the star formation efficiency can be expressed as  $\text{SFE}' = \text{SFE}'_i/t$ , with the star formation efficiency per timescale ( $\text{SFE}'_i$ ) being constant, then the quantity  $(L'_{\text{CO}}/\text{SFR})/t$  should be also constant for the timescale ‘ $t$ ’ regardless of the SFR of the system. This can be understood as a constant depletion time per timescale unit. We test this in Fig 13 by showing our proxy of the depletion time divided by the orbital time  $[(L'_{\text{CO}}/\text{SFR})/t_{\text{orb}}]$  and the crossing time  $[(L'_{\text{CO}}/\text{SFR})/t_{\text{cross}}]$ . Both panels are plotted against the SFR.

We can see in the left panel of Fig 13 how our proxy of depletion time per orbital time varies with SFR. The Spearman’s rank correlation coefficient is  $-0.30$  with a significance of  $0.004$ . We also get a best-fit power-law slope of  $-0.64 \pm 0.09$ . As mentioned before, this trend may be enhanced by pressure support effects which increase the observed orbital time (by decreasing  $V_{\text{rot}}$ ) as  $\sigma_v$  becomes comparable to  $V_{\text{rot}}$ . On the other hand, in the right panel of Fig 13 we can see that our proxy of depletion time per crossing time appears to be independent of the SFR. The Spearman’s rank correlation coefficient is  $-0.003$  with a significance of  $0.98$ , suggesting not correlation between both quantities. This plot also suggests that  $L'_{\text{CO}}/\text{SFR} \approx t_{\text{cross}}$ , with a median value of  $\sim 1.7$  and the  $1\sigma$  region between  $\sim 0.8$  and  $4.8$ . This suggests  $\text{SFE}'_{t_{\text{cross}}} \sim 1$ .

We note that a constant star formation efficiency per crossing time found in our work departs from the fixed efficiency per free-fall time suggested by Krumholz, Dekel & McKee (2012), as their estimation of the free-fall time for their extragalactic data set varies with the rotational velocity ( $t_{\text{ff,T}} \propto \Omega^{-1} \propto V_{\text{rot}}^{-1}$ ). Nevertheless, in the  $V_{\text{rot}}/\sigma_v \approx 1$  limit, the free-fall time calculated by Krumholz, Dekel & McKee (2012) becomes comparable with the crossing time ( $t_{\text{cross}} \approx \Omega^{-1}$ ). Thus, both laws fit the extragalactic data as

a simple linear function in the  $V_{\text{rot}}/\sigma_v \gtrsim 1$  range. A possible way to differentiate both laws would be by performing spatially resolved molecular gas observations in star-forming galaxies with  $V_{\text{rot}}/\sigma_v < 1$ , where  $t_{\text{ff,T}} > t_{\text{cross}}$ .

Our finding also does not contradict numerical simulations in which it is found that the star formation efficiency is ‘well-represented’ by an exponentially decreasing function of the angular velocity of the disk (Utreras, Becerra & Escala 2016).

Before finalising this study, we would like to caution that spatial resolution effects may affect our analysis of Fig. 12 and Fig 13. Indeed, the low spatial resolution of our observations may lead to an overestimation of  $t_{\text{orb}}$  through possible overestimated CO half-light radii and underestimated  $V_{\text{rot}}$  (§ 3.7). This effect might decrease the estimated gas consumption rate per orbital time, especially on the sources observed at lower spatial resolution, which also are the galaxies with greater pressure support and higher  $r_{1/2,\text{CO}}$  values within our sample. We note that the slope of the best-fit for the  $\text{SFR}-L'_{\text{CO}}/\tau_{\text{orb}}$  correlation gets lower ( $N = 0.87 \pm 0.09$ ) if we just consider galaxies observed with a projected beam size lower than  $5\text{ kpc}$  within our sample. This spatial resolution limit is, for example, the value obtained for the current seeing limited ( $\sim 0''.6$ ) IFS observations at  $z \sim 1$ . We also note that this spatial resolution threshold selects ‘normal’ star-forming galaxies, but just one starburst galaxy with  $V_{\text{rot}}/\sigma_v \approx 2$  at  $z < 0.06$  within our resolved sample. In this case, all of the selected galaxies have  $\text{SFR} \lesssim 12 M_{\odot} \text{ yr}^{-1}$ . Thus, our conclusion remains unchanged.

On the other hand,  $t_{\text{cross}}$  may be less affected by spatial resolution effects as both,  $\sigma_v$  and  $r_{1/2,\text{CO}}$  values tend to be overestimated. If we consider the galaxies observed with a projected beam size lower than  $5\text{ kpc}$  within our sample, we found a best-fit slope for the  $\text{SFR}-L'_{\text{CO}}/\tau_{\text{cross}}$  correlation of  $1.13 \pm 0.17$ . However, as we mentioned earlier, this thresh-

old just include one starburst galaxy with low  $V_{\text{rot}}/\sigma_v$  ratio and SFR. When we include galaxies observed with a spatial resolution up to 7 kpc (six more galaxies;  $V_{\text{rot}}/\sigma_v \sim 1$ ;  $\text{SFR} \lesssim 20 M_{\odot} \text{ yr}^{-1}$ ), we obtain a slope of  $1.23 \pm 0.12$ . In summary, our results are dependent whether we consider the systems with high SFRs and lower  $V_{\text{rot}}/\sigma_v$  ratios. Regardless of the spatial resolution effects discussed recently, the variable  $\alpha_{\text{CO}}$  factor should also have an affect on our analysis.

## 5 CONCLUSIONS

We present ALMA observations of 39 flux-selected ( $S_{160\mu\text{m}} \geq 100 \text{ mJy}$ ;  $L_{\text{IR}} \approx 10^{10-12} L_{\odot}$ ) galaxies with detected CO( $J = 1 - 0$ ) emission, comprising ‘starburst’ and ‘normal’ star-forming galaxies drawn from the VALES survey (V17), at the redshift range of  $0.02 < z < 0.35$ . We incorporate the exquisite multi-wavelength coverage from the GAMA survey. We found 20 galaxies with extended (‘resolved’) emission whilst 19 have ‘compact’ (or ‘unresolved’) emission. The spatial resolution of the sample ranges from 2 to 8 kpc, with a fixed spectral resolution of  $20 \text{ km s}^{-1}$ . We model the CO(1-0) kinematics by using a two-dimensional disk model with an arctan velocity profile and consider disk thickness effects on the projection of the galactic disk in the observed plane. These new observations represent one of the largest samples of molecular gas kinematics traced by the CO of ‘typical’ and ‘starburst’ star-forming galaxies at intermediate redshifts.

The median  $V_{\text{rot}}/\sigma_v$  ratio for our sample is 4.1 and the  $V_{\text{rot}}/\sigma_v$  values range between 0.6 – 7.5. We found median  $V_{\text{rot}}/\sigma_v$  ratios of 4.3 and 1.6 for the ‘normal’ star-forming and starburst sub-samples, respectively. The median  $V_{\text{rot}}/\sigma_v$  value for the ‘normal’ galaxies in our sample is consistent with the expected evolution with redshift for this ratio.

We find a tentative correlation between the  $L_{\text{IR}}$  luminosity with the rotation-to-pressure support ratio ( $V_{\text{rot}}/\sigma_v$ ). That anti-correlation suggest a smooth transition of the star formation efficiency on terms of the kinematic state for ‘starburst’ and ‘normal’ star-forming galaxies.

We find that the  $[\text{CII}]/\text{IR}$  ratio decreases at low  $V_{\text{rot}}/\sigma_v$  ratio. The data are well-represented by a power-law with best-fit slope of  $0.74 \pm 0.14$ . Our finding is consistent with Ibar et al. (2015) who found that galaxies presenting a prominent disk show higher  $L_{[\text{CII}]} / L_{\text{IR}}$  ratios than those which do not present disky morphologies. The VALES galaxies with  $V_{\text{rot}}/\sigma_v \gtrsim 3$  tend to show  $L_{[\text{CII}]} / L_{\text{IR}}$  comparable with the values measured in the KINGFISH survey for nearby galaxies (Smith et al. 2017), whilst galaxies with  $V_{\text{rot}}/\sigma_v \lesssim 3$  tend to show lower  $L_{[\text{CII}]} / L_{\text{IR}}$  values.

We compare the physical parameters derived by PDR modeling for our sample (Hughes et al. 2017a) with the  $V_{\text{rot}}/\sigma_v$  ratio. We find that high hydrogen nuclei densities and high strength of the FUV radiation field are likely to be found in systems with low  $V_{\text{rot}}/\sigma_v$  ratio, with the latter quantity being almost independent of the CO, [CII] luminosities used to constrain the PDR model.

By calculating dynamical masses following both, thin and thick turbulent disk models, we find that the thin disk model tends to underestimate the galactic total mass as its values are lower than the estimated stellar masses for five of our galaxies. On the other hand, the thick turbulent disk model tends to alleviate this conflict, suggesting that these

sources with low  $V_{\text{rot}}/\sigma_v$  values are better represented by thick galactic disks. This also suggests that pressure support effects should not be neglected in high velocity dispersion galactic disks. We caution that this conclusion is strongly dependent on the spatial resolution of our observations.

We test if our rotationally supported galaxies are prone to develop gravitational instabilities. This is done by analysing our sources in the  $f_{\text{H}_2} - V_{\text{rot}}/\sigma_v$  plane and comparing with expected values for a marginally stable gaseous thin disk ( $Q_{\text{gas}} = 1$ ), a gaseous thick disk ( $Q_{\text{thick}} = 1$ ) and a two component disk (stars plus gas;  $Q_2 = 1$ ). From 11 galaxies classified as rotationally supported systems, we find that three galaxies are consistent with  $Q_{\text{gas}} \approx 1$ , i.e., are prone to develop gravitational instabilities. The other eight systems have measured  $Q_{\text{gas}} \gtrsim 1$ . This conclusion is not changed if we apply the thick disk gravitational stability analysis as the kinematics estimates are not enough accurate. The gravitational analysis considering a galactic disk with both, a gaseous and stellar component, may change this result by increasing the number of galaxies consistent with being susceptible to develop gravitational instabilities, however stellar dynamics measurements are needed to corroborate this result.

We explore the possible origin of the energy sources of those high turbulent motions seen in our galaxies by comparing the SFRs with  $f_{\text{H}_2}$  and  $\sigma_v$ . We find that the SFR is weakly correlated with  $f_{\text{H}_2}$ . By comparing the data with two theoretical models in the literature, the feedback-driven and gravity-driven models, we find that both models give a poor description of the data. This suggests that the main energy source of the supersonic turbulence observed in the VALES galaxies seem to be neither the gravitational energy released by cold gas accreted through the galactic disk nor the energy injected into the ISM by supernovae feedback.

We study the spatially integrated star formation law dependence on galactic dynamics, avoiding assumptions about the CO-to-H<sub>2</sub> conversion factor by studying the  $\text{SFR} - L'_{\text{CO}}/t_{\text{orb}}$  and  $\text{SFR} - L'_{\text{CO}}/t_{\text{cross}}$  relations. We find a correlation between SFR and  $L'_{\text{CO}}/t_{\text{orb}}$ , with a best-fit power-law slope of  $1.21 \pm 0.13$ . We suggest that the  $\text{SFR} - L'_{\text{CO}}/t_{\text{orb}}$  correlation is affected by the decrease of  $V_{\text{rot}}$  (thus, an increase of  $t_{\text{orb}}$ ) by pressure support which dilutes the gravitational potential in systems with low  $V_{\text{rot}}/\sigma_v$  ratio.

We find that our proxy of the ‘star formation efficiency’ ( $\text{SFE}' \propto \text{SFR}/L'_{\text{CO}}$ ) is correlated with the crossing time, suggesting an efficiency per crossing time of  $\sim 0.6$ . Therefore, by knowing the size, SFR, and mean velocity dispersion of a galaxy, we can estimate its molecular gas mass. By considering the better correlation between  $\text{SFE}'$  and  $t_{\text{cross}}$ , we propose that the crossing time may be the timescale in which the star formation occurs in our systems. We caution, however, that the assumption of a CO-to-H<sub>2</sub> conversion factor and/or spatial resolution effects may change this result.

Obtain deeper and higher resolution observations of the molecular gas in a large sample of highly turbulent systems is critical to confirm or refute the findings reported in our work. It will allow to overcome spatial resolution effects which bias the velocity dispersion to higher values and to characterise the rotational velocity of the systems by observing the flat part of the velocity curve. This will be done in future work.

## ACKNOWLEDGEMENTS

We thank the referee for her/his careful reading and useful comments. We acknowledge to L. Cortese and P. Papadopoulos for their generous discussions and useful comments. This research was supported by CONICYT Chile (CONICYT-PCHA/Doctorado-Nacional/2014- 21140483) E.I. acknowledges partial support from FONDECYT through grant N° 1171710. This paper makes use of the following ALMA data: ADS/JAO.ALMA#2012.1.01080.S, ADS/JAO.ALMA#2013.1.00530.S and ADS/JAO.ALMA#2015.1.01012.S. ALMA is a partnership of ESO (representing its member states), NSF (USA) and NINS (Japan), together with NRC (Canada), MOST and ASIAA (Taiwan), and KASI (Republic of Korea), in cooperation with the Republic of Chile. The Joint ALMA Observatory is operated by ESO, AUI/NRAO and NAOJ. CONICYT grants Basal-CATA PFB-06/2007 (FEB) and FONDECYT Regular 1141218 (FEB); the Ministry of Economy, Development, and Tourism's Millennium Science Initiative through grant IC120009, awarded to The Millennium Institute of Astrophysics, MAS (FEB). A.M.M.A. acknowledges support from CONICYT through FONDECYT grant 3160776. M.J.M. acknowledges the support of the National Science Centre, Poland through the POLONEZ grant 2015/19/P/ST9/04010; this project has received funding from the European Union's Horizon 2020 research and innovation programme under the Marie Skłodowska-Curie grant agreement No. 665778. GDZ acknowledges support by the ASI/Physics Department of the university of Roma-Tor Vergata agreement n. 2016-24-H.0 for study activities of the Italian cosmology community. This publication has received funding from the European Union's Horizon 2020 research and innovation programme under grant agreement No 730562 [RadioNet]. C.C. was supported from the Chinese Academy of Sciences (CAS) through the CASSACA Postdoc Grant, by the Visiting Scholarship Grant administered by the CAS South America Center for Astronomy (CASSACA), NAOC and by the Young Researcher Grant of National Astronomical Observatories, Chinese Academy of Sciences. G.O. acknowledges the support provided by CONICYT (Chile) through FONDECYT postdoctoral research grant no 3170942. C.Y. was supported by an ESO Fellowship. T.M.H. acknowledges the support from the Chinese Academy of Sciences (CAS) and the National Commission for Scientific and Technological Research of Chile (CONICYT) through a CAS-CONICYT Joint Postdoctoral Fellowship administered by the CAS South America Center for Astronomy (CASSACA) in Santiago, Chile.

## REFERENCES

- Bell, E. F., van der Wel, A., Papovich, C., et al. 2012, *ApJ*, 753, 167
- Belloocchi, E., Arribas, S., & Colina, L. 2012, *A&A*, 542, 54
- Bershady, M., Verheijen, M., Swaters, R., et al. 2010, *ApJ*, 716, 198
- Bertin, E. & Arnouts, S. 1996, *A&AS*, 117, 393
- Bigiel, F., Leroy, A., Walter, F., et al. 2008, *AJ*, 136, 2846
- Bolatto, A. D., Wolfire, M. & Leroy, A. K. 2013, *ARA&A*, 51, 207
- Bolatto, A. D., Wong, T., Utomo, D., et al. 2017, *ApJ*, 846, 159
- Bothwell, M. S., Smail, I., Chapman, S. C., et al. 2013, *MNRAS*, 429, 3047
- Bourne, N., Dunne, L., Maddox, S. J., et al. 2016, *MNRAS*, 462, 1714
- Bournaud, F., Elmegreen, B. G. & Martig, M. 2009, *ApJ*, 707, 1
- Bruce, V. A., Dunlop, J. S., Cirasuolo, M., et al. 2012, *MNRAS*, 427, 1666
- Burkert, A., Genzel, R., Bouché, N., et al. 2010, *ApJ*, 725, 2324
- Burkert, A., Förster Schreiber, N. M., Genzel, R., et al. 2016, *ApJ*, 826, 214
- Chabrier, G. 2003, *PASP*, 115, 763
- Charbonneau, P. 1995, *ApJS*, 101, 309
- Cheng, C., Ibar, E., Hughes, T., et al. 2017, *MNRAS*, 475, 248
- Courteau, S. 1997, *AJ*, 114, 2402
- da Cunha, E., Charlot, S., Elbaz, D., et al. 2008, *MNRAS*, 388, 1595
- Daddi, E., Elbaz, D., Walter, F., et al. 2010, *ApJL*, 714, 118
- Davies, R., Förster Schreiber, N. M., Cresci, G., et al. 2011, *ApJ*, 741, 69
- Dalgarno, A. & McCray, R. A., 1972, *ARA&A*, 51, 105
- de Blok, W., Walter, F., Brinks, E., et al. 2008, 136, 2648
- Díaz-Santos, T., Armus, L., Charmandaris, V., et al. 2014, *ApJ*, 774, 68
- Dickman, R. L. 1978, *ApJS*, 37, 407
- Dickman, R. L., Snell, R. L. & Schloerb, F. P. 1986, *ApJ*, 309, 326
- Di Teodoro, E. M., Fraternali, F. & Miller, S. H. 2016, *A&A*, 594, 77
- Downes, D., Solomon, P. M. & Radford, S. J. E. 1993, *ApJ*, 414, 13
- Downes, D. & Solomon, P. M. 1998, *ApJ*, 507, 615
- Draine, B. & Li, A. 2007, *ApJ*, 657, 810
- Driver, S. P., Wright, A. H., Andrews, S. K., et al. 2016, *MNRAS*, 455, 3911
- Eales, S., Dunne, L., Clements, D., et al. 2010, *PASP*, 122, 499
- Elmegreen, B. G. 2011, *ApJ*, 737, 10
- Epinat, B., Amram, P., Balkowski, C., & Marcelin, M. 2010, *MNRAS*, 401, 2113
- Epinat, B., Tasca, L., Amram, P., et al. 2012, *A&A*, 539, 92
- Escala, A. & Larson, R. B. 2008, *ApJ*, 685, 31
- Faucher-Giguère, C., Quataert, E. & Hopkins, P. 2013, *MNRAS*, 433, 1970
- Förster Schreiber, N. M., Genzel, R., Bouché, N., et al. 2009, *ApJ*, 706, 1364
- Gnerucci, A., Marconi, A., Cresci, G., et al. 2011, *ApJ*, 533, 124
- Genzel, R., Burkert, A., Bouché, N., et al. 2008, *ApJ*, 687, 59
- Genzel, R., Newman, S., Jones, T., et al. 2011, *ApJ*, 733, 101
- Genzel, R., Tacconi, L., Lutz, D., et al., 2015, *ApJ*, 800, 20
- Glazebrook, K. 2013, *PASA*, 30, 56
- Green, A., Glazebrook, K., McGregor, P., et al. 2010, *Natur*, 467, 684
- Green, A., Glazebrook, K., McGregor, P., et al. 2014, *MNRAS*, 437, 1070
- Griffin, M., Abergel, A., Abreu, A., et al. 2010, *A&A*, 518, 3
- Goldreich, P. & Lynden-Bell, D. 1965, *MNRAS*, 130, 97
- Gullberg, B., De Breuck, C., Vieira, J. D., et al. 2015, *MNRAS*, 449, 2883
- Habing, H. J. 1968, *Bull. Astron. Inst. Netherlands*, 19, 421
- Harrison, C., Johnson, H., Swinbank, A. M., et al. 2017, 467, 1965
- Häußler, B., McIntosh, D. H., Barden, M., et al. 2007, *ApJS*, 172, 615
- Heyer, M., Krawczyk, C., Duval, J. & Jackson, J. M. 2009, *ApJ*, 699, 1092
- Holmberg, E. 1958, *MeLuS*, 136, 1
- Hopkins, P. F. 2012, *MNRAS*, 423, 2016
- Hughes, T., Ibar, E., Villanueva, V., et al. 2017a, *A&A*, 602, 49

- Hughes, T., Ibar, E., Villanueva, V., et al. 2017b, *MNRAS*, 468, 103
- Ibar, E., Lara-López, M. A., Herrera-Camus, R., et al. 2015, *MNRAS*, 449, 2498
- Jog, C. J. & Solomon, P. M. 1984, *ApJ*, 276, 114
- Jog, C. J. 1996, *MNRAS*, 278, 209
- Johnson, H., Harrison, C., Swinbank, A., et al. 2018, *MNRAS*, 474, 5076
- Kassin, S. A., Weiner, B. J., Faber, S. M., et al. 2012, *ApJ*, 758, 106
- Kaufman, M. J., Wolfire, M. G., Hollenbach, D. J., & Luhman, M. L. 1999, *ApJ*, 527, 795
- Kaufman, M. J., Wolfire, M. G., Hollenbach, D. J., & Luhman, M. L. 1999, *ApJ*, 527, 795
- Kaufman, M. J., Wolfire, M. G., & Hollenbach, D. J. 2006, *ApJ*, 644, 283
- Kramer, C., Abreu-Vicente, J., García-Burillo, S., et al. 2013, *A&A*, 553, 114
- Kelvin, L. S., Driver, S. P., Robotham, A. S. G., et al. 2012, *MNRAS*, 421, 1007
- Kennicutt, R. C. 1998a, *ApJ*, 498, 541
- Kennicutt, R. C. 1998b, *AR&A*, 36, 189
- Kennicutt, R. C., Calzetti, D., Walter, F., et al. 2007, *ApJ*, 671, 333
- Kennicutt, R. C., Calzetti, D., Aniano, G., et al. 2011, *PASP*, 123, 1347
- Krumholz, M. R., & McKee, C. F. 2005, *ApJ*, 630, 250
- Krumholz, M. R. & Tan, J. 2007, *ApJ*, 654, 304
- Krumholz, M. R., Dekel, A., & McKee, C. F. 2012a, *ApJ*, 745, 69
- Krumholz, M. R. & Burkhardt, B. 2016, *MNRAS*, 468, 1671
- Larson, R. B. 1981, *MNRAS*, 194, 809
- Lang, P., Wuyts, S., Somerville, R. S., et al. 2014, *ApJ*, 788, 11
- Law, D. R., Steidel, C. C., Shapley, A. E., et al. 2012, *ApJ*, 85, 85
- Lehnert, M., Nesvadba, N., Le Tiran, L., et al. 2009, *ApJ*, 699, 1660
- Leroy, A., Walter, F., Brinks, E., et al. 2008, *AJ*, 136, 2782
- Leroy, A., Walter, F., Bigiel, F., et al. 2009, *AJ*, 137, 4670
- Leroy, A., Walter, F., Sandstrom, K., et al. 2013, *AJ*, 146, 19
- Liske, J., Baldry, I. K., Driver, S. P., et al. 2015, *MNRAS*, 452, 2087
- Lowe S., Roberts W., Yang J., et al. 1994, *ApJ*, 427, 184
- Madden, S. C., Geis, N., Genzel, R., et al. 1993, *ApJ*, 407, 579
- Malhotra, S., Helou, G., Stacey, G., et al. 1997, *ApJ*, 491, 27
- Malhotra, S., Kaufman, M. J., Hollenbach, D., et al. 2001, *ApJ*, 561, 766
- Mogotsi, K., de Blok, W., Caldú-Primo, A., et al. 2016, *AJ*, 151, 15
- Molina, J., Ibar, E., Swinbank, A. M., et al. 2017, *MNRAS*, 466, 892
- Mosenkov, A., Sotnikova, N., Reshetnikov, V., et al. 2015, *MNRAS*, 451, 2376
- Narayanan, D., Krumholz, M., Ostriker, E., & Hernquist, L. 2012, *MNRAS*, 421, 3127
- Neugebauer, G., Habing, H. J., van Duinen, R., et al. 1984, *ApJ*, 278, 1
- Nozawa, T. & Kozasa, T. 2013, *ApJ*, 776, 24
- Oberst, T. E., Parshley, S. C., Stacey, G. J., et al. 2006, *ApJL*, 652, 125
- Papadopoulos, P. P., Seaquist, E. R. 1999, *ApJ*, 516, 114
- Papadopoulos, P., van der Werf, P., Xilouris, E., et al. 2012, *ApJ*, 751, 10
- Peng, C. Y., Ho, L. C., Impey, C. D. & Rix, H. 2010, *AJ*, 139, 2097
- Pilbratt, G., Riedinger, J., Passvogel, T., et al. 2010, *A&A*, 518, 1
- Pineda, J. L., Langer, W. D., Velusamy, T., et al. 2013, *A&A*, 554, 103
- Pineda, J. E., Langer, W. D. & Goldsmith, P. F. 2014 *A&A*, 570, 121
- Poglitsch, Waelkens, C., Geis, N., et al. 2010, *A&A*, 518, 2
- Rafikov, R. R. 2001, *MNRAS*, 323, 445
- Röllig, M., Abel, N. P., Bell, T., et al. 2007, *A&A*, 467, 187
- Romeo, A. B. 1992, *MNRAS*, 256, 307
- Romeo, A. B., Burkert, A. & Agertz, O. 2010, *MNRAS*, 407, 1223
- Romeo, A. B. & Wiegert, J. 2011, *MNRAS*, 416, 1191
- Romeo, A. B. & Falstad, N. 2013, *MNRAS*, 433, 1389
- Saintonge, A., Lutz, D., Genzel, R., et al. 2013, *ApJ*, 778, 2
- Schaye, J., Crain, R. A., Bower, R. G., et al. 2015, *MNRAS*, 446, 521
- Schmidt, M. 1959, *ApJ*, 129, 243
- Sérsic, J. L., *BAAA*, 6, 41
- Shapiro, K., Genzel, R., Förster Schreiber, N., et al. 2008, *ApJ*, 193, 335
- Shetty, R., Glover, S., Dullemond, C., et al. 2011b, *MNRAS*, 415, 3253
- Silk, J. 1997, *ApJ*, 481, 703
- Smith, J. D. T., Croxall, K., Draine, B., et al. 2017, *ApJ*, 834, 5
- Solomon, P. M., Rivolo, A. R., Barrett, J. & Yahil, A. 1987, *ApJ*, 319, 730
- Solomon, P. M., Downes, D., Radford, S. J. E. & Barrett J. W. 1997, *ApJ*, 478, 144
- Solomon, P. M., & Vanden Bout, P. A., 2005, *ARA&A*, 43, 677
- Springel, V., & Hernquist, L., 2003, *MNRAS*, 339, 289
- Stacey, G., Geis, N., Genzel, R., et al. 1991, *ApJ*, 373, 423
- Stacey, G. J., Hailey-Dunsheath, S., Ferkinhoff, C., et al. 2010a, *ApJ*, 724, 957
- Stott, J. P., Swinbank, A. M., Johnson, H. L., et al. 2016, *MNRAS*, 457, 1888
- Swinbank, A. M., Sobral, D., Smail, I., et al. 2012a, *MNRAS*, 426, 935
- Swinbank, A. M., Smail, I., Sobral, D., et al. 2012b, *ApJ*, 760, 130
- Swinbank, A. M., Harrison, C. M., Trayford, J., et al. 2017, *MNRAS*, 467, 3140
- Tielens, A. & Hollenbach, D. 1985, *ApJ*, 291, 722
- Toomre, A., 1964, *ApJ*, 139, 1217
- Turner, O., Cirasuolo, M., Harrison, C., et al. 2017, *MNRAS*, 471, 1280
- Utreras, J., Becerra, F. & Escala, A. 2016, *ApJ*, 833, 13
- Valiante, E., Smith, M. W. L., Eales, S., et al. 2016, *MNRAS*, 462, 3146
- Villanueva, V., Ibar, E., Hughes, T. M., et al. 2017, *MNRAS*, 470, 3775
- Vogelsberger, M., Genel, S., Springel, V., et al. 2014, *MNRAS*, 444, 1518
- Walter, F., Brinks, E., de Blok, W., et al. 2008, 136, 2563
- White, H., Fisher, D., Murray, N., et al. 2017, *ApJ*, 846, 35
- Wisnioski, E., Glazebrook, K., Blake, C., et al. 2012, *MNRAS*, 422, 3339
- Wisnioski, E., Förster Schreiber, N. M., Wuyts, S., et al. 2015, *ApJ*, 799, 209
- Wong, T., & Blitz, L. 2002, *ApJ*, 569, 157
- Wright, E., Eisenhardt, P., Mainzer, A., et al. 2010, *AJ*, 140, 1868
- Wuyts, S., Förster Schreiber, N. M., van der Wel, A., et al. 2011b, *ApJ*, 742, 96
- Zhou, L., Federrath, C., Yuan, T., et al. 2017, *MNRAS*, 470, 4573

## APPENDIX A: DYNAMICAL MASS WITH DIFFERENT DENSITY PROFILES

In § 4.4 we show that roughly half of the galaxies within our sample are best described by a thick disk model rather than a thin disk model. The thick disk dynamical model

predicts total masses greater than the stellar masses at the same radii unlike the thin disk dynamical model. However, in order to implement the thick disk model, the surface density of the source needs to be known. For our galaxies we assumed a surface density profile given by the observed surface density brightness in the  $K$ -band, but we also assume a constant mass-to-light ratio and light extinction over the galactic disk. This is likely not to be true since we expect a major concentration of dust (thus extinction) in the central part of galaxies compared to their outskirts. With the aim to show that our choice of surface density distribution should not affect the conclusions of § 4.4, in Fig. A1 we plot the ratio between the dynamical masses assuming an exponential surface density profile and our observational Sérsic-like surface density profile as a function of the  $V_{\text{rot}}/\sigma_v$  ratio. When assuming an exponential surface density profile, we obtain greater dynamical mass values on average compared to our observational Sérsic-like surface density profiles. However, the median ratio of  $\sim 1.5$  indicates that our conclusions should not be sensitive to the chosen surface density profiles. We note that the possible trend between the dynamical mass ratio and the  $V_{\text{rot}}/\sigma_v$  ratio observed in Fig. A1 is consistent with the finding of increasing Sérsic indices above unity at galaxies with  $\log(M_*/M_\odot) > 10.5$  (Wuyts et al. 2011; Bell et al. 2012; Lang et al. 2014). We also note that disk truncation is expected to be enhanced in galaxies with considerable turbulent pressure support (Burkert et al. 2016).

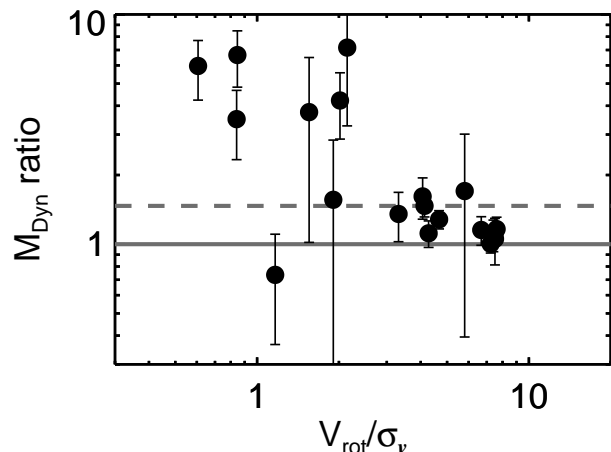


**Figure A1.** Ratio between the thick disk dynamical masses assuming an exponential surface density profile and our  $K$ -band converted surface density profile as a function of the  $V_{\text{rot}}/\sigma_v$  ratio for our sample. The grey line represents equality between both quantities. The dashed line represents the median value of  $\sim 1.5$  for our sample. By assuming an exponential surface density profile we obtain greater dynamical mass estimates. This seems to be dependent of the observed  $V_{\text{rot}}/\sigma_v$  ratio.

### APPENDIX C: KINEMATIC MAPS AND VELOCITY PROFILES

In Fig. C1 we plot the kinematic maps (1st to 3rd columns), residual maps (4th column) and one-dimensional velocity profiles (5th and 6th columns) for our sample taken from the VALES survey. Full information for the panels in the figure is given in its caption.

This paper has been typeset from a  $\text{\TeX}/\text{\LaTeX}$  file prepared by the author.

### APPENDIX B: EDGE-CALIFA SURVEY

In § 4.6, § 4.6 and § 4.7 we complement our analysis by adding the EDGE-CALIFA survey data (Bolatto et al. 2017) to our VALES data. The EDGE-CALIFA is survey based on interferometric CO(1–0) observations made with the Combined Array for Millimeter-wave Astromy (CARMA) of 126 nearby ( $d = 23 - 130$  Mpc) galaxies from the EDGE survey. This sample is selected from the CALIFA survey and it has on average spectral and spatial resolution of  $\sim 10 \text{ km s}^{-1}$  and  $\sim 1.4$  kpc, respectively. Those are higher spectral and spatial resolution observations than the ones presented in our survey (Table 2).

From the EDGE-CALIFA survey, we analyse the galactic kinematics of the galaxies which have available their CO intensity, velocity and dispersion velocity maps with the additional requirement that the velocity map must sample the galactic centre given from the SDSS ‘igu’ multi-color image. Thus, we ‘just’ analyse 70 galaxies from the EDGE-CALIFA survey. The kinematic analysis is done in the same manner than we did for the VALES survey, but with two differences; (1) we constrain the inclination angles by using the values presented in Bolatto et al. (2017); and (2) we model these galaxies as thin galactic disks, i.e.,  $q_0 = 0.0$ . Finally, we correct the gas mass content by using our chosen CO-to- $\text{H}_2$  conversion factor, and we correct the stellar masses and SFRs for a Chabrier IMF.

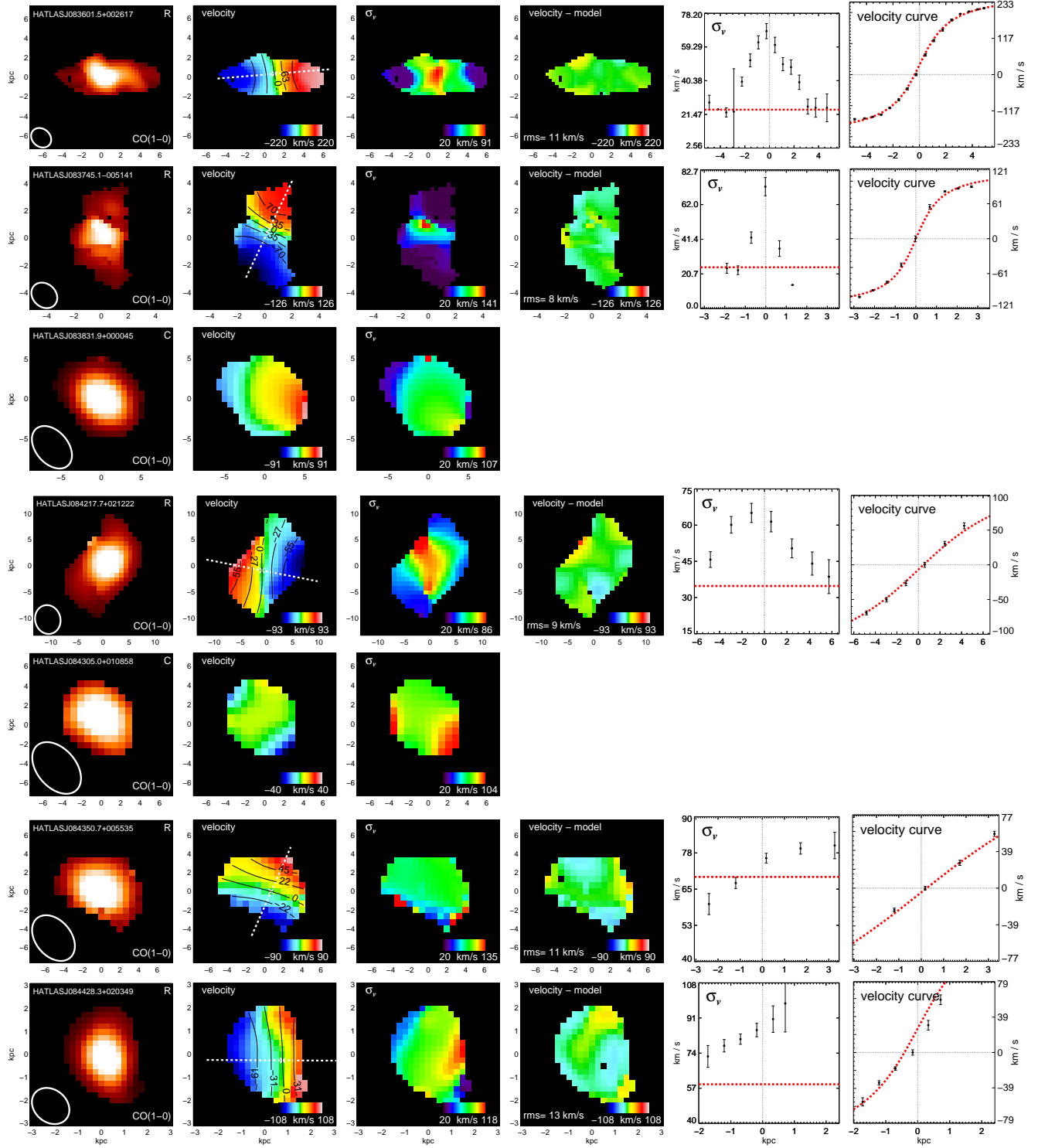


**Figure C1.** CO(1-0) intensity, velocity, LOS velocity dispersion ( $\sigma_v$ ), residual field, major axis velocity dispersion and velocity profiles (columns) for each target from our sample (rows). Each target is labelled as ‘resolved’ (R) or ‘compact’ (C) in their intensity map, ‘compact’ galaxies were not modelled (see §2.2 for more details). The map also shows the synthesized beam. The velocity field has overlotted the kinematic centre, the major kinematic axis and velocity contours from their best-fit disk model. The LOS velocity dispersion ( $\sigma_v$ ) field is corrected for the local velocity gradient ( $\Delta V/\Delta R$ ) across the synthesized beam. The residual map is constructed by subtracting the velocity disk model from the velocity map: the r.m.s. of these residuals are given in each panel. The one-dimensional profiles are derived from the two dimensional velocity fields using the best-fit kinematic parameters and a slit width with size equal to half of the beam FWHM across the major kinematic axis. In each one-dimensional profile, the error bars show the  $1\sigma$  uncertainty and the vertical dashed grey line represents the best-fit dynamical centre. In the velocity dispersion profile panels, the red-dashed line shows the mean galactic value (Table 2), whilst in the last column, the red-dashed curve shows also the best-fit for each source.



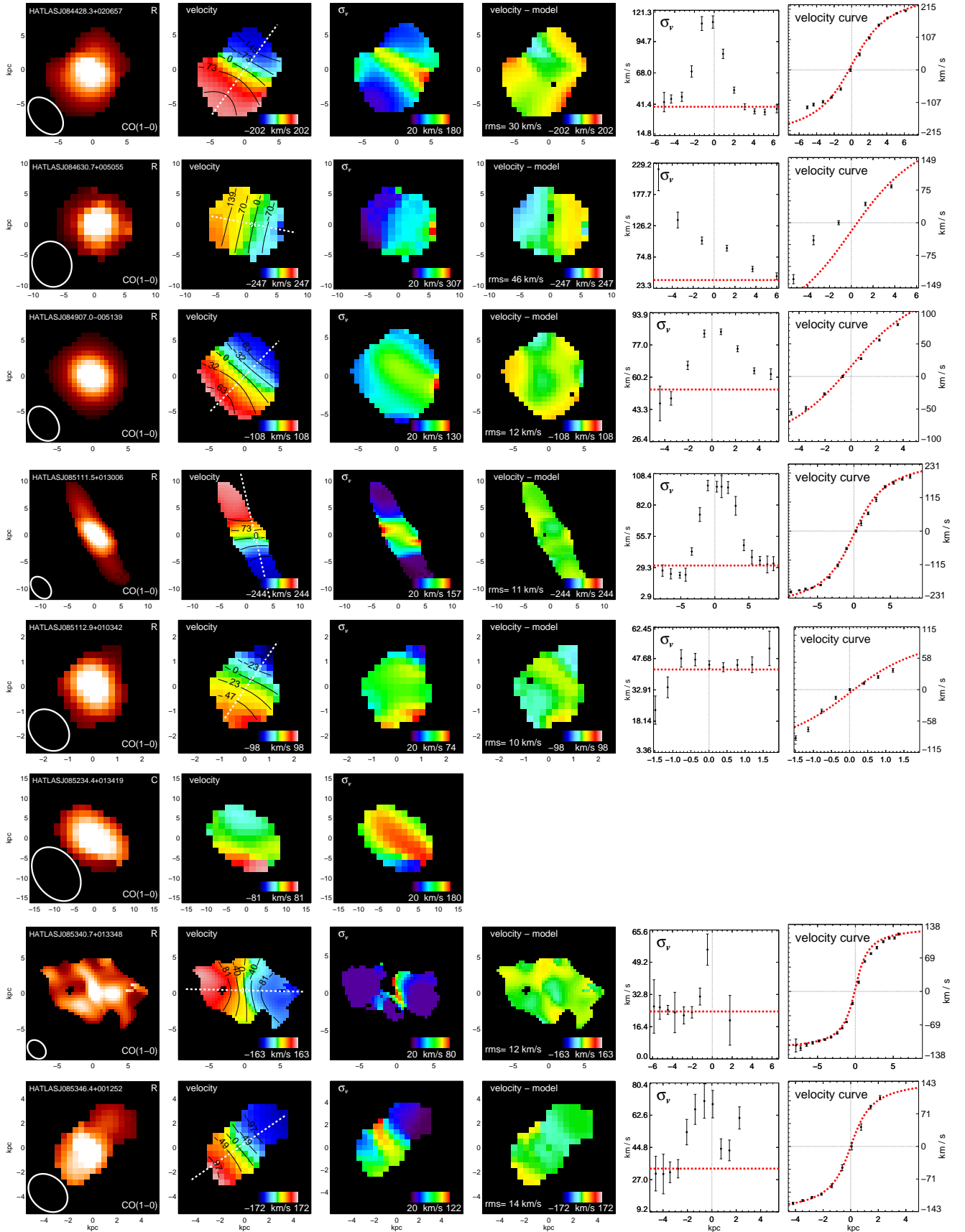


Figure C1. Continued.

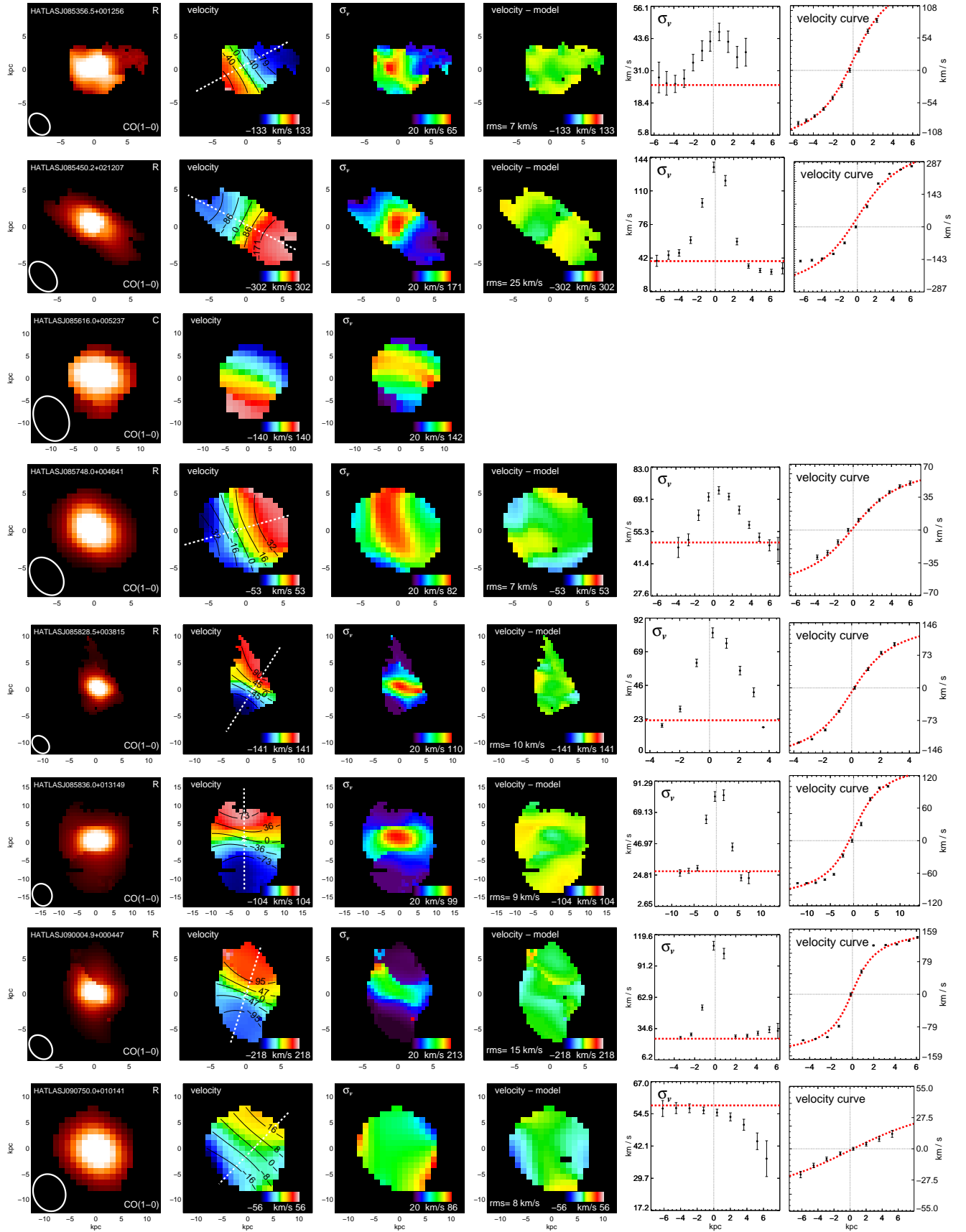


Figure C1. Continued.

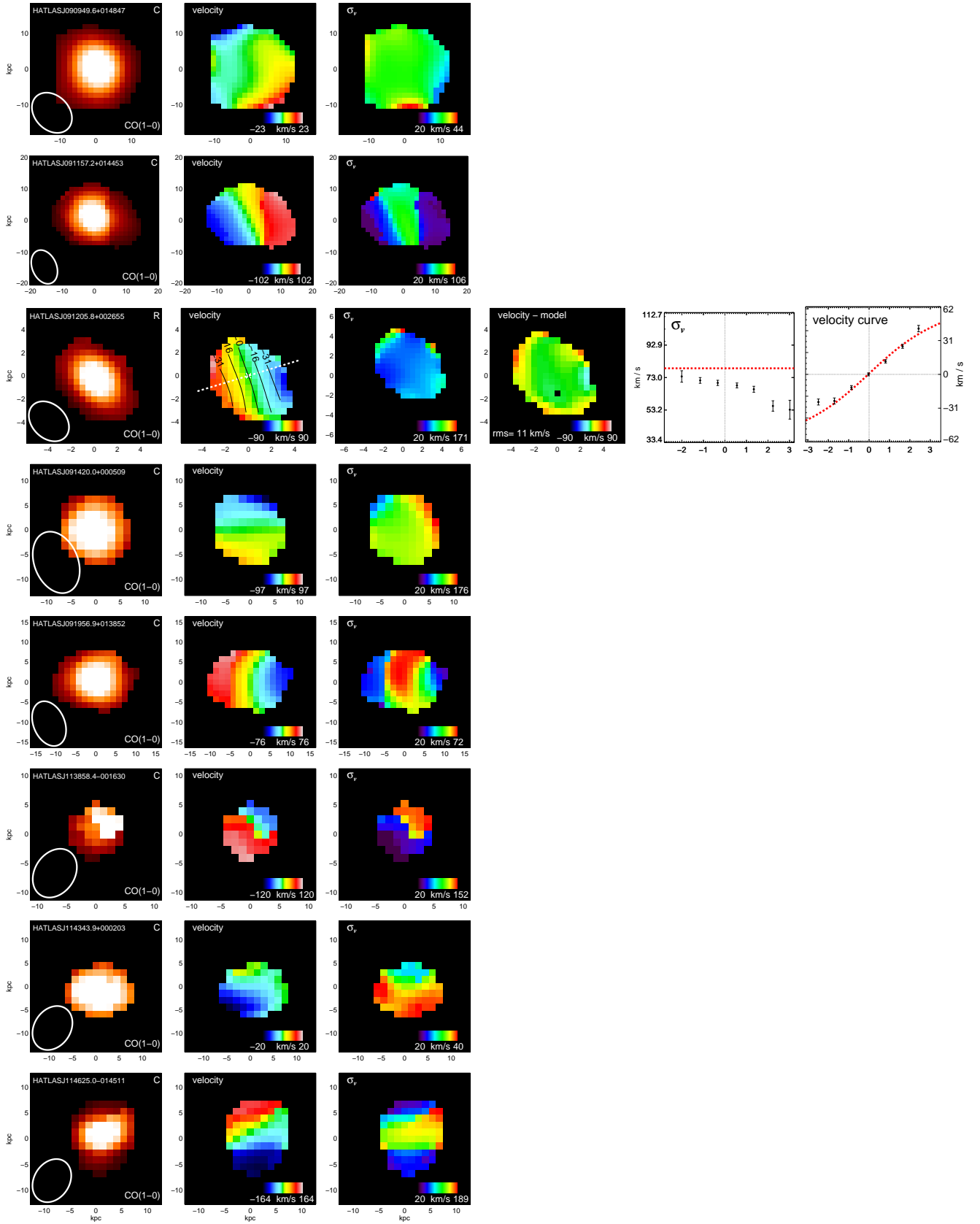


Figure C1. Continued.

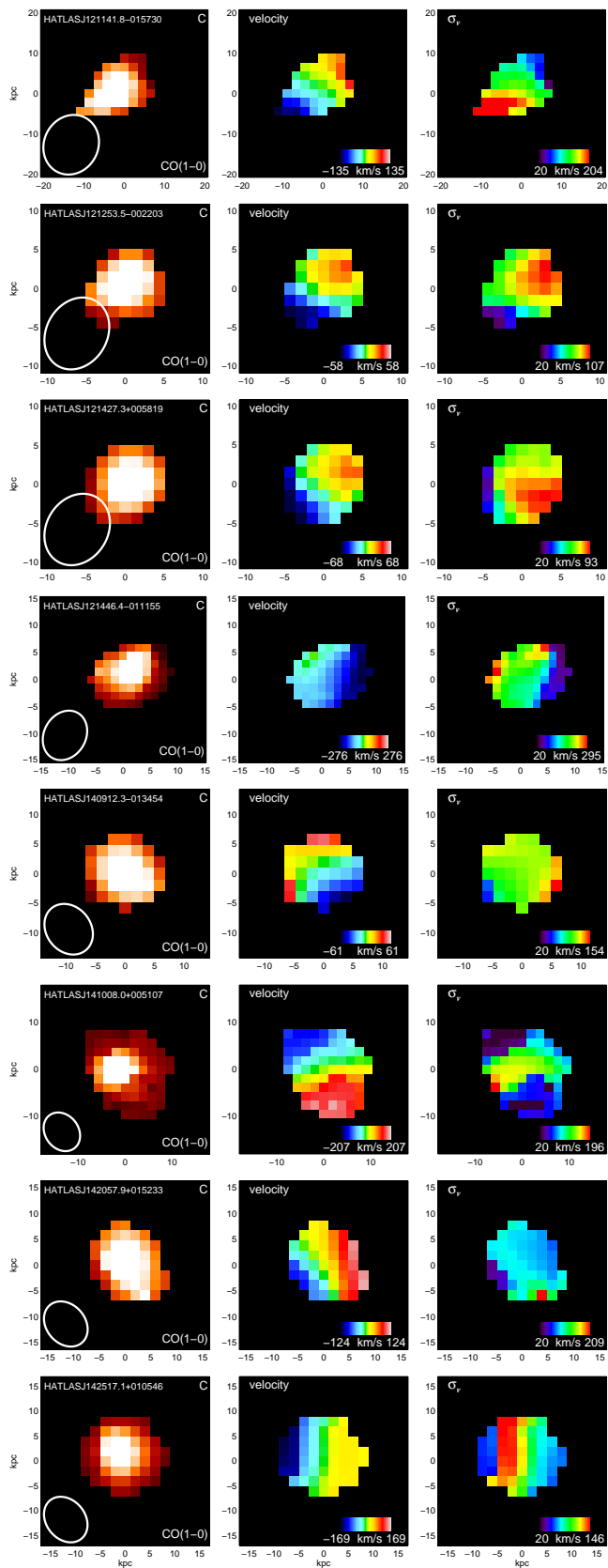


Figure C1. Continued.